Characterizing rotations in thermally-driven winds above a valley floor using observations from the 21 August 2017 solar eclipse and a climatological analysis

Ross Theodore Palomaki
Park City, UT

Bachelor of Science, Mathematics
Bachelor of Arts, Music
University of North Texas, 2013

A Thesis presented to the Graduate Faculty
of the University of Virginia in Candidacy for the Degree of
Master of Science

Department of Environmental Sciences
University of Virginia
August 2018

Acknowledgements

I would first like to thank my advisor, Stephan. Your guidance over these three years has helped me become a stronger writer and more capable scientist. Thank you for taking a chance on the new kid in town without the first clue about atmospheric science. I also wish to thank my committee members, Pat and Kevin, both for their assistance with this thesis project and for the excellent classes I was able to take from them.

This project would have been a complete disaster if not for the outstanding efforts of my lab mates. Thank you Nevio, Michael, Gert-Jan for all the early mornings and late nights, for the long days in the heat and humidity, for the installation and uninstallation and reinstallation of weather stations, and for the good times in the office, in the field, and at the bar. I feel very lucky to have worked, hiked, cycled, traveled, and human-corkscrewed alongside you guys.

I am also deeply grateful for the seemingly infinite love and support from my family and friends, especially Mom, Dad, Kya, and Lisa. To the Upstairs Crew of P^2 and MC+N: thank you for always being there to help add the life to my work-life balance. To my fellow EVSC graduate students: our tight-knit community is one of the most special aspects of this department. Thank you for three wonderful years of homework groups, practice presentations, pig roasts, frisbee teams, intellectual stimulation, and scientific inspiration. To Doug, who is lying next to me as I type this (and also to Sam): you're a good boy.

Finally, to Sarah: it's hard to believe that it's already been four years since you brought us out to Charlottesville. I think neither of us could have predicted the successes, failures, triumphs, and heartaches we have faced since then. Thank you for being right at my side throughout this sometimes bumpy ride. I couldn't ask for a better travel buddy as we wait to see where the journey will take us next.

Table of Contents

List of Tables

List of Figures

Abstract

Thermally-driven winds in complex terrain are characterized by a diurnal cycle with upvalley winds during the day, downvalley winds at night, and transitional periods around sunrise and sunset. These winds are important for air pollution dispersion in valleys, and can also affect weather patterns on a regional scale. However, the winds are not always resolved in weather and climate models, and poor parameterization schemes result in inaccurate weather forecasting over mountainous regions. Observations of thermally-driven winds during transition periods will help improve model parameterizations, and ultimately lead to more accurate weather forecasting in complex terrain.

The 21 August 2017 solar eclipse provided a unique opportunity to observe thermally-driven winds in a valley. The rapid decrease and subsequent increase in solar radiation created two transitionary periods in the middle of the afternoon. The wind patterns that emerged during and after the eclipse were similar to those during the morning and evening transitions, but with distinct differences due to the sun's position during the eclipse. The high elevation and low azimuth angles during the eclipse caused the wind over the valley floor to rotate between upvalley, downslope, and downvalley flows. The direction of these rotations (clockwise vs. counterclockwise) was strongly influenced by terrain features in the valley. A period of northeasterly wind between these rotations was unexpected as it does not align with the main southeast-northwest valley axis. Wind rotations over valley sidewalls have been described in previous studies, but rotations over valley floors are not well-documented in the literature.

A year-long dataset was examined in order to further investigate the significance of the the wind rotations and northeasterly wind observed during the eclipse. First, the data were filtered to identify thermally-driven days at the investigation area. Wind rotations and periods of northeasterly winds were flagged in this filtered dataset. Small wind rotations with magnitudes of 30 degrees or less occur frequently during the day and the night. Large rotations of 135 degrees or more occur much less often, and happen most frequently around sunrise and sunset. Northeasterly winds occur with the highest frequency during the morning transition period and coincide with large clockwise wind rotations. Hence, the northeasterly wind on the afternoon of 21 August was a direct result of the solar eclipse. Wind rotations appear frequently over the valley floor, and follow a diurnal cycle on thermally-driven days. These wind rotations could have important implications for air pollution dispersal in valleys.

Chapter 1

Introduction

Although there are many definitions of the atmospheric boundary layer (ABL), one simple definition is the part of the troposphere that is directly influenced by the presence of Earth's surface, and responds to surface forcings with a timescale of an hour or less (Stull 1988). The forcings that affect the ABL are numerous and interact in complex ways, resulting in feedback loops between radiation, surface heat fluxes, and meteorological variables at the surface and in the ABL (Ek and Mahrt 1994). The surface energy budget is driven by longwave and shortwave radiation received by the surface, which is balanced by heat flux between the surface and deeper soil, as well as turbulent fluxes of sensible and latent heat between the surface and the atmosphere. These turbulent fluxes are typically directed upward from the surface during the daytime and contribute to ABL heating and moistening. From a bulk perspective, turbulent fluxes can be estimated using gradients of temperature, humidity, and wind between Earth's surface and the air directly above the surface (typically measured at 2 m). Changes in downward radiation alter the surface temperature, which in turn alters the temperature gradient and ultimately the turbulent fluxes of sensible and latent heat to the ABL.

In regions of complex terrain, downward radiation also controls the presence and characteris-

tics of thermally-driven orographic winds, including slope and valley winds. Slope winds are driven by horizontal temperature (and therefore pressure) gradients that form between the air above a valley sidewall at a given elevation and the air above the center of a valley at the same elevation (Whiteman 2000). Valley winds are similarly driven by horizontal pressure gradients between the valley and the surrounding plains. Typically, these thermally-driven winds are directed upslope and upvalley during the daytime, with a reversal in direction at night. Vertical exchange processes associated with daytime thermally-driven winds can significantly modify weather on local and regional scales. For example, observational studies in deep Alpine valleys have shown that up to three times the valley air mass is exported vertically during the day under fair weather conditions through a process termed *mountain venting* (Kossmann et al. 1999; Henne et al. 2004). This is approximately equivalent to exporting 30% of the valley air mass per hour (Henne et al. 2005b), which includes aerosols, water vapor and air pollutants. Modeling studies have found elevated moisture and pollution layers that have been transported vertically above the ABL and into the free troposphere as a result of mountain venting (De Wekker et al. 2004; Henne et al. 2005a).

Some of the largest changes in the ABL occur during the morning and evening transition periods as a result of radiation forcing when the sun rises and sets. Thus, previous studies on ABL dynamics and evolution over all terrain types have focused considerable attention on these transition periods (e.g. Lenschow et al. 1979; Mahrt 1981; Angevine et al. 2001; Lothon et al. 2014). Many investigations of the ABL within valleys center around the evolution of slope and valley winds during these times. In a valley, the morning transition period begins when incoming shortwave radiation exceeds outgoing longwave radiation, and ends with the breakup of the surface-based temperature inversion that forms overnight (Whiteman 1982; Zardi and Whiteman 2013). The time required for winds to reverse during the transition period depends on the dimensions of the valley (Whiteman et al. 1989; Pardyjak et al. 2009), and also on the spatial scale of the flow (i.e. slope vs. valley winds; see Zardi and Whiteman 2013). Previous studies have observed slope winds (Nadeau et al. 2013) and valley winds

(Duine et al. 2017) to reverse direction on the order of 10-60 min. In other cases, the onset of upvalley wind does not occur until several hours after sunrise (Whiteman 1989; Weigel and Rotach 2004; Pal et al. 2014). Additionally, wind reversal may occur on different timescales between the morning and evening transitions in a given valley.

Motivation for detailed investigations of the valley ABL response to changes in radiative forcing is to improve model parameterization schemes of exchange processes in unresolved valleys. Many current climate and weather models, particularly GCMs, are run at spatial scales that are too coarse to resolve each individual peak and valley in a mountain range. Unresolved terrain is not inherently problematic, as long as the effects of the missing terrain features are adequately parameterized inside the model. However, many parameterization schemes, especially those for the ABL and turbulence, are based upon data collected over flat terrain and are not always appropriate for use in complex topography (Zhong and Chow 2013). Improper parameterization schemes applied to mountainous regions can introduce errors in model output, resulting in cold biases (Chin et al. 2001; Awan et al. 2011; Gao et al. 2015) or underestimated diurnal temperature ranges (Kalverla et al. 2016), surface-based temperature inversions that are too weak (Hanna and Yang 2001; Zhong and Fast 2003), and biases in surface wind speed (Jiménez et al. 2010; Jiménez and Dudhia 2011) or wind direction (Michioka and Chow 2008; Jiménez and Dudhia 2013). These errors and biases can drastically reduce the accuracy of weather and air quality forecasts in regions of complex terrain.

A solar eclipse provides an exceptional opportunity to study the response of the ABL to changes in radiative forcing. Meteorological observations during solar eclipse events date back to the 19th century (a comprehensive list of more than 100 articles is given by Aplin et al. 2016). While many studies have focused on temperature changes during eclipse events, winds have also been the subject of some investigation, beginning with correspondence between Clayton (1901) and Bigelow (1902). Since these early reports, additional observational (Gross

and Hense 1999; Piriou and Lamboley 1999; Prenosil 2000) and modeling studies (Founda et al. 2007; Gray and Harrison 2012) have examined regional and synoptic wind patterns that arise during eclipse events. One result that has emerged from these studies of wind during eclipse events is a disruption in the thermally-driven land-sea breeze caused by eclipse-induced cooling (Gross and Hense 1999; Bala Subrahamanyam and Anurose 2011). It follows that local changes to thermally-driven slope and valley winds can be expected over the time span of a partial or total solar eclipse (∼2-3 hours).

Previous studies have briefly described modifications to orographic winds as a result of eclipse-induced cooling. Fernández et al. (1993) attributed wind patterns recorded at several surface weather stations in Costa Rica during the 11 July 1991 eclipse to local orographic flows. Vogel et al. (2001) simulated the 11 August 1999 eclipse over a small domain centered on southern Germany, and found significant changes in wind speed and direction near the mountainous regions in the domain. Anderson (1999) suggested that rapid changes in orographic winds could be partially responsible for anecdotal reports of the *eclipse wind*, a sudden increase in wind speed at totality. More recently, Eugster et al. (2017) used data from 165 surface weather stations in Switzerland to examine temperature and wind changes during the 20 March 2015 solar eclipse, which was only a partial eclipse over the study area. The cooling from this partial eclipse was sufficient to delay or prevent the morning transition to upvalley flows at stations situated on valley floors. They also noted large variability in wind direction at several weather stations installed near valley sidewalls, but discarded the data from these stations during their regional analysis of wind changes.

These results indicate that cooling from even a partial solar eclipse can alter the typical diurnal cycle of thermally-driven surface winds within a valley. However, the existing literature tends to disregard or only briefly mention this high variability in wind direction. Additionally, the vertical extent of these changes has not been investigated during previous eclipse events.

The primary goal of this thesis project is to observe thermally-driven winds in a valley during the 21 August 2017 solar eclipse. To this end, a field campaign is designed to investigate the effect of eclipse-induced cooling on changes in speed and direction of the valley wind at the surface and aloft. Instead of discarding highly variable wind direction data, this project focuses on it specifically. The remainder of this thesis is organized as follows:

- **Chapter 2** presents details of the field campaign and observations collected on 21 August. This chapter seeks to address the following research objectives:

    1. Investigate the effect of eclipse-induced cooling (and subsequent warming) on thermally-driven winds at the surface of a valley.

    2. Investigate the vertical extent of changes in wind speed or direction above the valley floor.

- **Chapter 3** presents a climatological analysis of meteorological data from the field site in order to better contextualize the observations collected during the eclipse event. This chapter seeks to address the following research objectives:

    1. Identify thermally-driven days at the field site that occurred over the course of one year.

    2. Compare observations collected during the eclipse to those collected during diurnal transition periods on thermally-driven days.

    3. Identify synoptic weather patterns that may allow for the development of thermally-driven flows at Innisfree.

- **Chapter 4** summarizes the main results and conclusions of the thesis.

- **Appendix A** provides a description of additional instrumentation that was installed in the investigation area during the eclipse, but was not used as part of the analysis in

Chapter 2.

- **Appendix B** shows a comparison of temperature sensors and anemometers installed on the main tower in the investigation area.
- **Appendix C** details a calibration experiment for some of the instruments used during the eclipse experiment in Chapter 2.

Chapter 2

The effect of a solar eclipse on thermally-driven flows in a small valley

This chapter will be submitted for publication in *Theoretical and Applied Climatology* with the following citation:

Palomaki, R.T., N. Babič, G.-J. Duine, M. van den Bossche, and S. F. J. De Wekker. The effect of a solar eclipse on thermally-driven winds in a small valley.

The manuscript is printed here, including the abstract and acknowledgements. References are combined with those from other chapters at the end of the thesis document.

Abstract

Thermally-driven winds in mountainous terrain exhibit a diurnal cycle of upvalley winds during the day, downvalley winds at night, and transitional periods around sunrise and sunset. On the afternoon of 21 August 2017 a partial solar eclipse occurred over the Blue Ridge Mountains in central Virginia, USA. High-resolution meteorological observations were made on the floor of a small valley to investigate the effect of eclipse-induced cooling on thermally-driven winds. Measurements taken both at the surface and in the lower atmosphere indicate cooling throughout much of the atmospheric boundary layer. Multiple surface weather stations observed wind rotations that occurred both during and after the eclipse, as winds shifted from upvalley to downslope and back to upvalley. The direction of these rotations (clockwise vs. counterclockwise) varied between stations and was strongly influenced by the proximity of the stations to topographic features in the valley. Lidar observations over the valley floor show a 300 m thick layer of downvalley winds that formed below a deeper layer of upvalley winds. These observations provide evidence that a daily wind rotation, typically described over valley sidewalls, may also exist at sites over valley floors.

2.1 Introduction

Meteorological observations during solar eclipse events date back to the 19th century, when Birt (1836) recorded changes in cloud cover during a partial solar eclipse over the United Kingdom. A comprehensive summary of historical eclipse weather observations is given by Aplin et al. (2016), who cite more than 100 articles. Some meteorological variables respond similarly across multiple solar eclipses. For example, temperature near the surface generally drops during the first half of an eclipse, then begins to rise again shortly after totality. However, the response of near-surface winds has been less consistent across eclipse events.

Clayton (1901) was the first to propose that a solar eclipse could affect mesoscale wind patterns. Based on observations of pressure, temperature, and winds during the May 28, 1900 eclipse, he concluded that the eclipse caused the formation of a "cold-air cyclone". He described an increase in gustiness during the eclipse as different sections of the cyclone pass over an observer. Bigelow (1902) disputed this explanation, claiming that the cooling effect of the moon's shadow was not sufficient to generate large-scale cyclonic flow. Instead, he hypothesized that the cooling altered the thermally-driven land-sea circulation near Clayton's coastal observation site.

Modeling studies have provided evidence that the effect of a solar eclipse on winds is strongest in regions characterized by spatial surface variability. Simulations of the 11 August 1999 solar eclipse over central Europe (Gross and Hense 1999; Prenosil 2000) showed the largest changes in wind speed and direction near the coastlines. Gross and Hense (1999) described the modelled wind field as 'a large scale land-sea circulation modified by orographic influences.' Modifications to land-sea circulations were also clearly visible in simulations of this eclipse over France (Piriou and Lamboley 1999, their Figure 7).

Anomalies in land-sea circulations during solar eclipses have also been confirmed by observational studies. During several eclipse events (e.g. Founda et al. 2007; Gray and Harrison

2012), significant shifts in winds were recorded by weather stations in close proximity to bodies of water. In a more comprehensive study of the land-sea circulation, Bala Subrahamanyam and Anurose (2011) collected measurements at the surface and aloft at a coastal site in India during the 15 January 2010 total solar eclipse, which began in the late morning hours at the study site. The sea breeze that developed on the eclipse day was weaker at the surface and was approximately 50% of the vertical thickness compared to a non-eclipse control day. Additionally, the onset of the evening land breeze occurred two hours earlier than on the control day.

These modelling and observational studies indicate that land-sea circulations are susceptible to influence from a solar eclipse. Thermally-driven orographic winds have not been studied to the same extent as land-sea circulations during solar eclipses. These orographic winds exist at spatial scales from a single slope to an entire mountain range, and are caused by differential heating between the atmosphere over the mountains and over the adjacent plains (Whiteman 2000). The winds form a diurnal pattern with upslope and upvalley winds during the day and downslope and downvalley winds at night. Transitional periods occur around the time the surface energy budget reverses sign (typically around sunrise and sunset). The time required for winds to reverse during the transition period depends on the dimensions of the valley (Whiteman et al. 1989; Pardyjak et al. 2009), and also on the spatial scale of the flow (Zardi and Whiteman 2013). Previous studies have observed slope winds (Nadeau et al. 2013) and valley winds (Duine et al. 2017) to reverse direction on time scales of 10-60 min. Hence, local changes to slope and valley winds are expected over the time span of a partial or total solar eclipse ($\sim$2-3 hours).

Previous studies have briefly described modifications to orographic winds as a result of solar eclipses. Fernández et al. (1993) attributed wind patterns recorded at several surface weather stations during the 11 July 1991 eclipse to local thermally-driven flows. Vogel et al. (2001) simulated the 11 August 1999 eclipse over a small domain centered on southern Germany.

They found significant changes in wind speed and direction near the mountainous regions in the domain, with minimal modifications to the wind field over homogeneous terrain. Anderson (1999) suggested that rapid changes in thermally-driven orographic winds could be partially responsible for the anecdotal reports of the *eclipse wind*, a sudden increase in wind speed at totality. Eugster et al. (2017) used data from 165 surface weather stations in Switzerland to examine temperature and wind changes during the 20 March 2015 solar eclipse. Even though the eclipse was only partial in Switzerland, the cooling was sufficient to delay or prevent the morning transition to upvalley flows.

While eclipse-induced changes in thermally-driven orographic flows have been observed at the surface, the vertical extent of these changes has not been investigated. Upvalley and downvalley winds typically extend vertically throughout the depth of the valley (Zardi and Whiteman 2013) with large changes in the flow structure around the morning and evening transition times (Zardi and Whiteman 2013; Lothon et al. 2014). A solar eclipse creates conditions that simulate an evening transition immediately followed by a morning transition, providing an opportunity to study the evolution of the valley boundary layer around the transition times in a quasi-laboratory setting.

On 21 August 2017 a total solar eclipse passed over the continental US from Oregon to South Carolina.[1] Eclipse literature separates a total solar eclipse into four phases. First contact occurs when the moon first moves between the earth and the sun. Second contact refers to the time that totality begins (i.e. the sun is entirely obscured by the moon), and third contact is when totality ends. Fourth (or final, last) contact occurs when the moon no longer obscures the sun. During a partial solar eclipse, only first and final contact occur. The goal of the present study was to observe thermally-driven orographic winds in a small valley during a partial eclipse. Specifically, we investigated the effect of eclipse-induced cooling on changes in speed and direction of the valley wind at the surface and aloft. To this end, we collected

[1]More information about the eclipse, including maps of the path of totality, can be found at https://eclipse2017.nasa.gov/

observations both at the surface and in the boundary layer which are presented in this paper. We first provide a description of the site in Section 2.2, followed by instrumentation details in Section 2.3. We then present and discuss the observations collected on 21 August in Section 2.4. Finally, we propose a hypothesis to explain the boundary layer response in Section 2.5. Section 2.6 contains a summary and conclusions.

2.2 Site description

The investigation area is situated in a small valley in the foothills of the Blue Ridge Mountains, ∼25 km northwest of Charlottesville, Virginia at an altitude of 314 m above mean sea level (MSL). The valley is oriented NNE-SSW and is ∼10 km long and 5 km wide (Figure 2.1). Ridges to the east are ∼700 m MSL, with ridges to the west of ∼850 m MSL. Observations were collected in an open, gently rolling farm field on the western side of the valley floor. The terrain immediately adjacent to the investigation area is highly complex. A small hill several hundred meters northeast of the site extends ∼100 m above the valley floor. Previous measurements taken in the investigation area have revealed that the hill affects local wind flow. Prevailing upvalley wind during the day is from the southeast, while downvalley wind at night is from the northwest (see Figure 6 in Pal et al. 2014). Downslope winds can reach the investigation area from both the small hill and the western valley sidewall. In the analysis of wind direction below, upvalley wind refers to wind from the southeast, and downvalley wind refers to wind from the northwest; hill downslope wind refers to downslope wind from the northeast, and sidewall downslope wind refers to downslope wind from the west (Figure 2.2).

The investigation area was ∼500 km northeast of the path of totality of the 21 August solar eclipse. A partial eclipse with a maximum solar obscuration of 85.7% occurred over the investigation area. First contact occurred at 13:14 EDT (local time; UTC-04:00), maximum

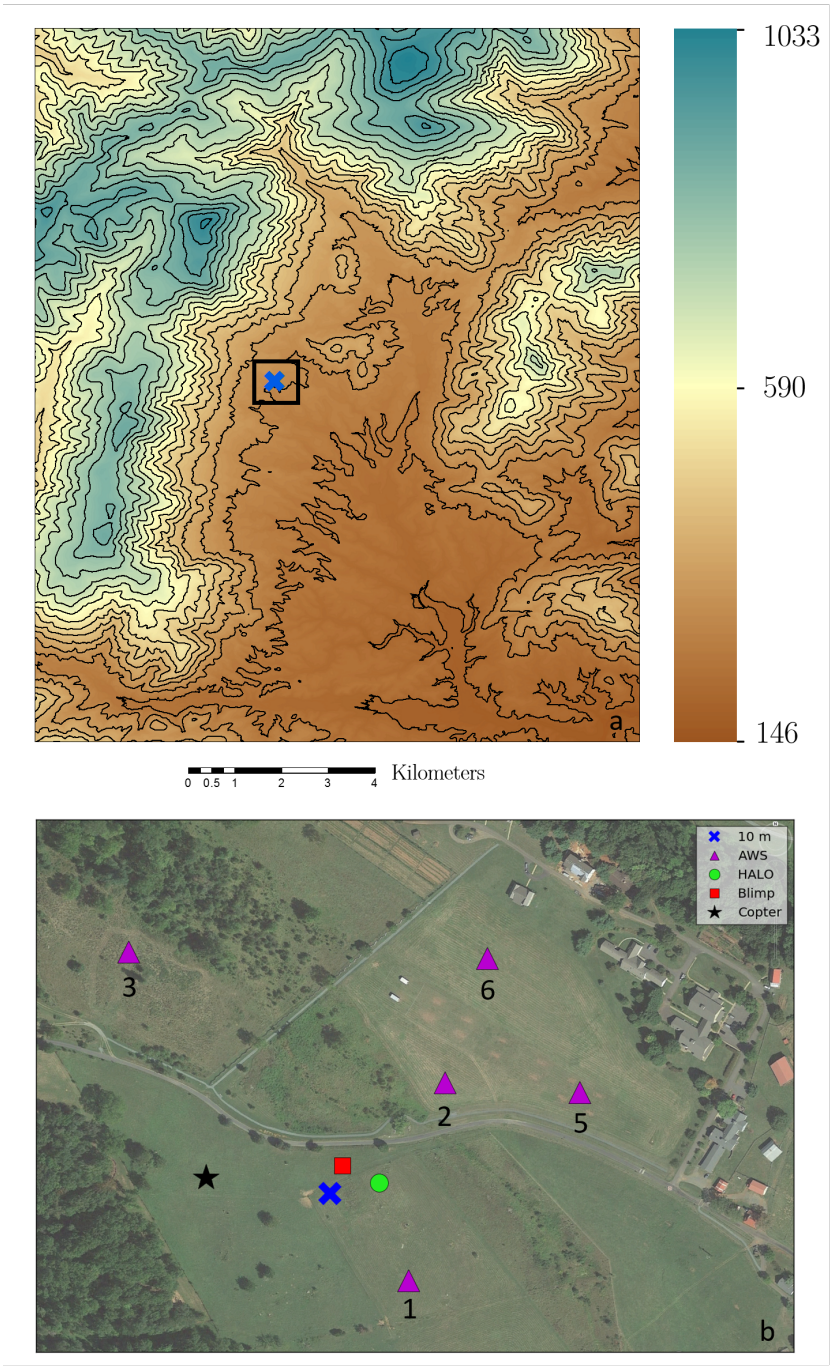

Figure 2.1: a) Topography surrounding our investigation area. The location of main tower in the valley is marked with a blue X. The black square denotes the area shown in the bottom panel. Shading indicates elevation in meters above mean sea level. b) Instrument locations at the investigation area. Five automated weather stations (AWS) were deployed for this study. Numbers labelling individual AWS are the same numbers used to describe them in the text.

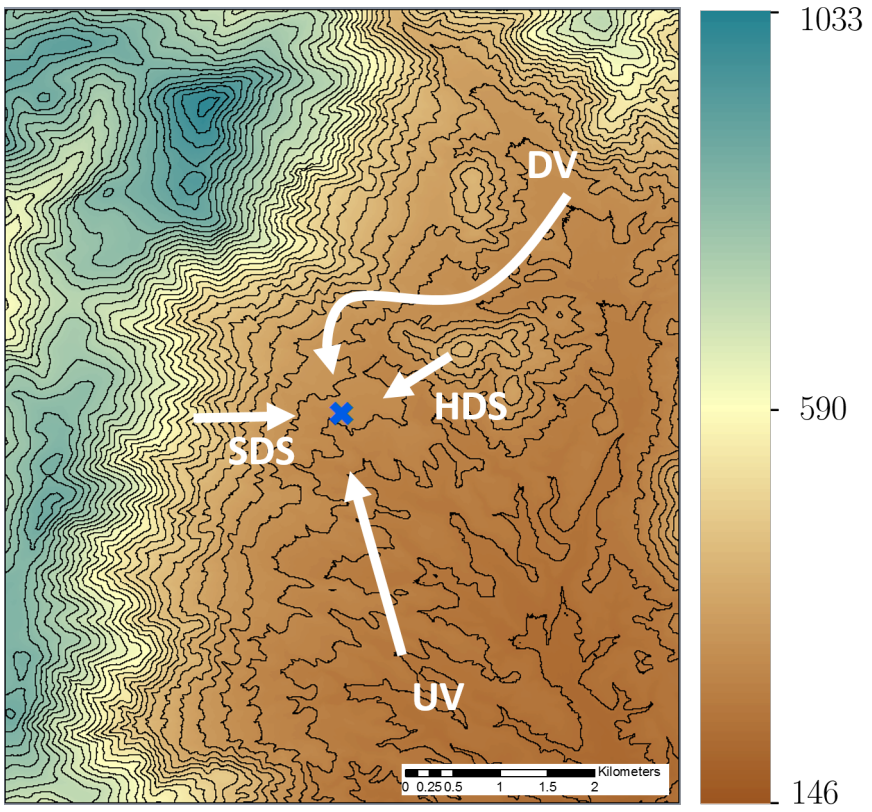

Figure 2.2: Prevailing wind patterns around the investigation area. Upvalley (UV) wind from the southeast; downvalley (DV) wind from the northwest; sidewall downslope (SDS) wind from the west; hill downslope (HDS) wind from the northeast. Shading indicated elevation in meters above mean sea level.

eclipse at 14:41 EDT, and final contact at 16:01 EDT, for a total duration of 2:45. Local sunrise was 07:01 EDT and sunset was 18:50 EDT.

2.2.1 Synoptic conditions

The investigation area was under the influence of high pressure during 20 and 21 August, with westerly winds of about 5 m s^{-1} at 850 hPa (Figure 2.3). In the early afternoon hours of 21 August, several small thunderstorm systems were present in the region (Figure 2.4), with precipitation recorded several kilometers to the south of the investigation area during the eclipse event. The eclipse was not obstructed by thunderstorm clouds at the actual investigation area, and no precipitation was recorded over the area on 21 August. Timelapse photos of cloud cover at the investigation area during the eclipse event are available in the online supplemental material.

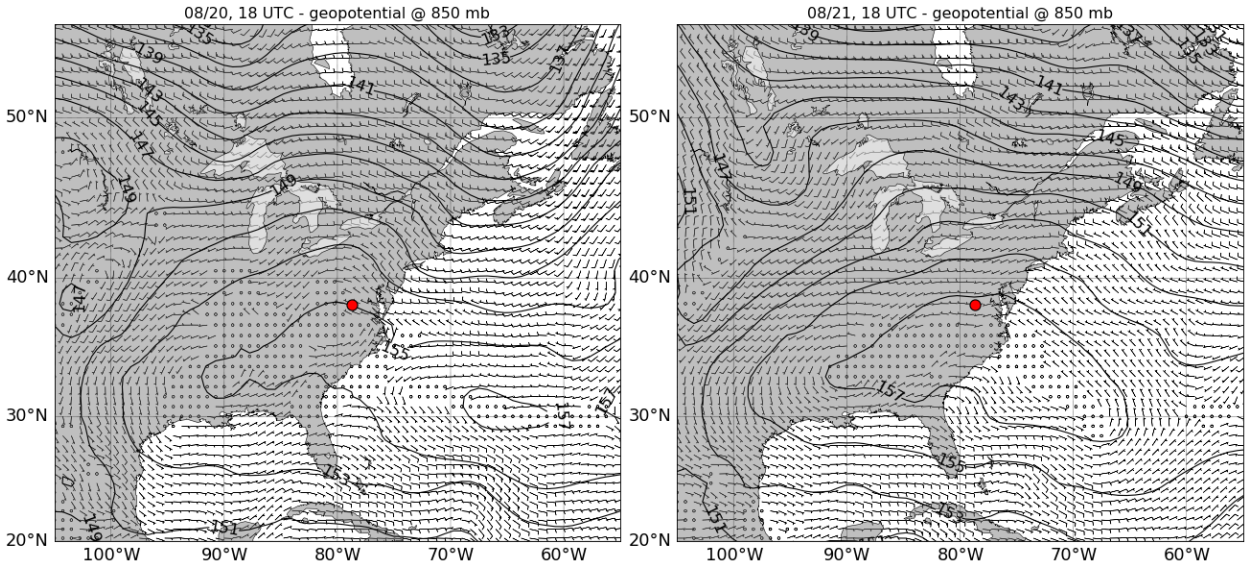

Figure 2.3: Synoptic weather conditions on 20 and 21 August 2017. Geopotential heights are given in decameters above mean sea level. The location of the main tower is marked by the red dot. Data from ECMWF reanalysis.

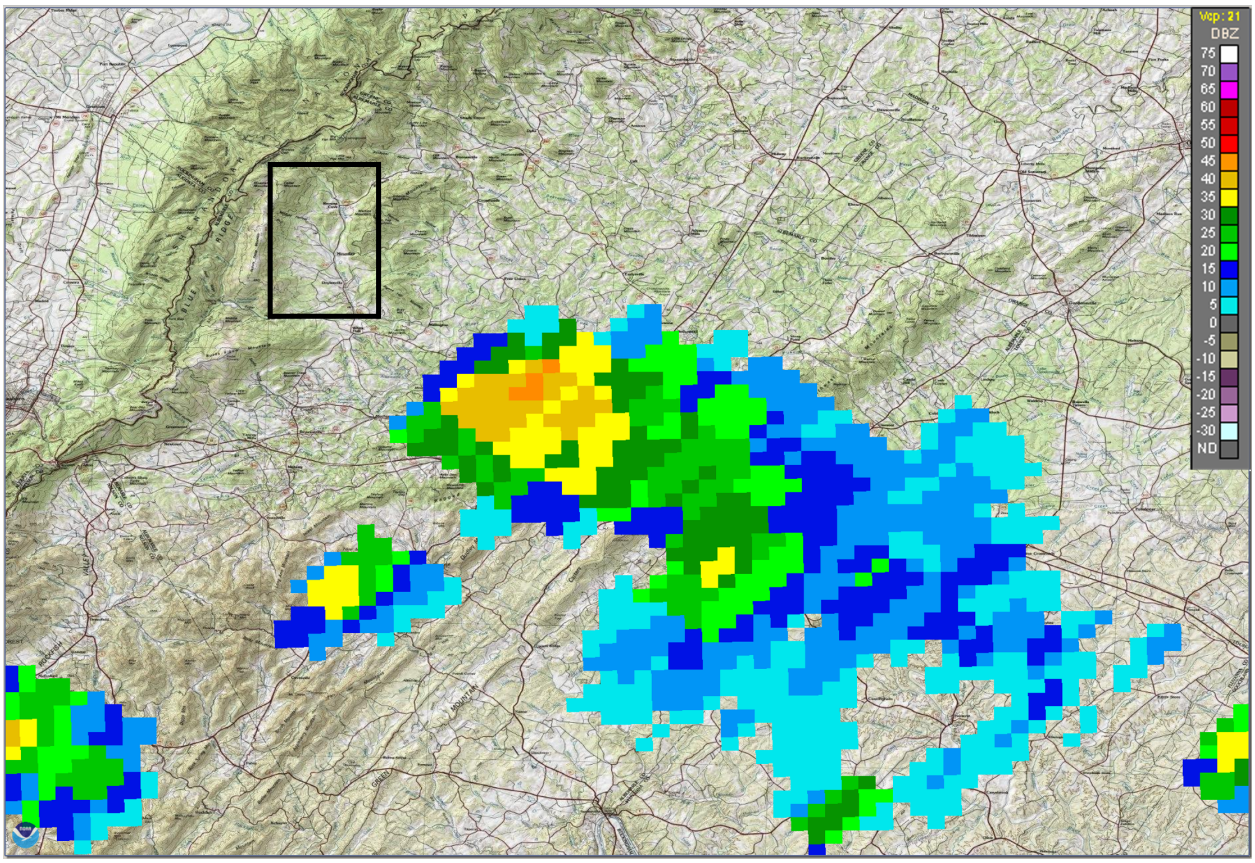

Figure 2.4: Composite radar reflectivity from NWS radar in Sterling, VA at 14:38 EDT on 21 August (3 min before maximum eclipse at the investigation area). The black box denotes the area shown in Figure 2.1a. Figure created using the NOAA Weather and Climate Toolkit, version 4.1.0.

2.3 Instrumentation and data collection

Figure 2.1b shows the layout of instrumentation at the investigation area. Descriptions of each instrument are provided below, with a summary of the details in Table 2.1.

Table 2.1: Abbreviations: temperature (T), relative humidity (RH), surface temperature (T_S), infrared (IR), shortwave/longwave radiation (SW and LW; incoming and outgoing components indicated with up and down arrows, respectively), wind speed (WS), wind direction (WD), three-dimensional wind components (u, v, w), sonic temperature (T_{son}),

Instrument	Sensor	Variable	Meas. height [m AGL]	Rate [Hz]
Main tower	Apogee ST110 thermistor	T	2.0, 9.4	1.0
	Onset S-THB-M002 thermohygrometer	T, RH	2.0, 9.4	1.0
	Apogee SIF-111 IR radiometer	T_S	3.5	0.2
	Apogee SN500	$SW^{\downarrow}$, $SW^{\uparrow}$, $LW^{\downarrow}$, $LW^{\uparrow}$	7.0	0.2
	RM Young Wind Monitor AQ propeller anemometer	WS, WD	9.8	1.0
	Gill Windmaster 3D sonic anemometer	u, v, w, T_{son}	10.0	20
AWS	Decagon DS-2	u, v	2.3	1.0
	Sensirion SHT15	T, RH	1.8	0.2
	Bosch BMP180	P	1.0	1.0
Lidar	HALO Photonics Stream Line	WS, WD, σ_w	100+	varied
Tethered balloon	Kestrel 4500 Weather Tracker	T, RH, P, WS, WD	0-100	0.5
Radiosonde	Graw DFM-09	T, RH, P, WS, WD	0-2500	0.2

2.3.1 Main tower

The 10 m main tower is centrally located in the investigation area (Figure 2.1). The instrumentation includes two shielded, mechanically aspirated thermistors at 2.0 and 9.4 m above ground level (AGL); two shielded, naturally ventilated thermohygrometers at 2.0 and 9.4 m AGL (temperature observations from these instruments were not used for analysis); a four-component net radiometer; a downward-facing infrared radiometer to measure surface temperature mounted at 3.5 m AGL; and a 3-dimensional sonic anemometer at 10 m AGL, and a propeller anemometer at 9.8 m AGL (observations from the propeller anemometer were not used for analysis). The sampling rates for these instruments during the observation period ranged from 0.2 Hz for the net radiometer to 20 Hz for the sonic anemometer (see Table 2.1). The raw 20 Hz sonic anemometer data are block-averaged to 10 Hz to reduce computational costs and aliasing effects (Kaimal and Finnigan 1994). Post-processing of the raw sonic anemometer data includes removal of questionable data and associated outliers (Vickers and Mahrt 1997), rotation of the measured wind speed components into the direction of the mean wind using the double rotation procedure (Kaimal and Finnigan 1994; Wilczak et al. 2001) and linear detrending to obtain the perturbations of the longitudinal velocity u', lateral velocity v', vertical velocity w' and sonic temperature T'_{son}. The sonic anemometer data are also used to calculate sensible heat flux H and turbulent kinetic energy (TKE). For these variables, standard block averages of 30 minutes do not provide the level of detail necessary to see changes during the eclipse. We present observations of H and TKE every minute, with each observation calculated as a 30-minute average that considers the 15 minutes before and after a given observation.

2.3.2 AWS

Five Automated Weather Stations (AWS) were deployed at distances ranging from 100 to 300 m from the main tower site to monitor the impact of the solar eclipse on local surface

meteorological properties at a high spatial and temporal resolution. These AWS were previously described by van den Bossche and De Wekker (2016), and consisted of a 2-D sonic anemometer to record wind speed and direction at 1 Hz, and sensors to monitor air temperature and humidity at 0.2 Hz and barometric pressure at 1 Hz, all at a height of 2 m AGL. We focus on analysis of the wind direction observations from these five AWS in Section 2.4.

2.3.3 Doppler lidar

To supplement the ground-based observations, we used a scanning Doppler wind lidar (StreamLine XR, Halo Photonics Ltd. UK), located approximately 20 m east of the main tower (Figure 2.1b). Due to power supply restrictions on 21 August, the lidar was running only during the morning transition (05:39-10:39 EDT), eclipse (11:52-16:54 EDT), and evening transition (17:26-22:30 EDT). The lidar was configured to provide vertical profiles of horizontal wind speed and direction every 80 s at a vertical resolution of 29 m, starting at a height of 100 m AGL. We calculated the horizontal wind speed and direction by applying the Velocity Azimuth Display (VAD) algorithm to the radial velocities at each range gate (Browning and Wexler 1968). Similar to Päschke et al. (2015), we used $n = 12$ azimuthal points with an elevation angle of 75 degrees. At each azimuthal point, 30000 pulsed laser beams of 1.5 μm wavelength were fired, resulting in a dwelling time of approximately 5 s. After each VAD scan pattern, a vertical stare was obtained, which provided vertical wind speed.

2.3.4 Tethered balloon profiles

Vertical profiles of temperature, humidity, pressure, and winds from the surface to 100 m were captured using a tethered balloon system during the afternoon and evening hours on 21 August. The system used in this project included a handheld weather meter (Nielsen-

Kellerman Kestrel 4500 Pocket Weather Tracker), a wind vane, and a 4 m long helium blimp, similar to the setup used by McKendry et al. (2009) and Phelps (2014). Attached to one horizontal end of the cross-shaped wind vane is a large plastic tail which allows the vane to point into the prevailing wind. A holster for the weather meter is attached to the opposite horizontal end, which secures the weather meter to the wind vane without obstructing the unit's impeller. The top of the wind vane is attached to the underside of the blimp with a 20 m length of rope. The bottom end is attached to a long rope, which is reeled around a winch.

To collect the vertical profiles, 100 m of rope was unwound from the winch at a rate of 10 m every 90 s, which allowed the blimp to carry the wind vane and weather meter up from the surface. The sampling rate of the weather meter was 0.5 Hz. Each ascent lasted 15 min, and data collected during the descents were discarded. For analysis, we bin the ascending data by height, with each bin representing the average over 5 m of altitude. During some profiles, the temperature sensor was not well aspirated in the first 5-10 m. Therefore, we exclude the first 10 m of temperature measurements in all profiles from our analysis, and instead use observations from the main tower in the vertical profiles. For each profile, temperature measured at 2 m and 10 m is time-averaged over the duration of the ascent, and these values are used in the first and second bins, respectively.

2.3.5 Radiosondes

Three Graw DFM-09 radiosondes were launched during the eclipse on 21 August: one close to first contact (actual launch time 13:16 EDT), the second at maximum eclipse (14:41 EDT), and the third close to final contact (15:59 EDT). The radiosondes provided vertical profiles of potential temperature and specific humidity that extend beyond the tethered balloon profiles near the surface. The first two soundings were terminated at an altitude of 5-6 km in order to prepare for subsequent launches. In the following discussion, we focus on the temperature

and humidity profiles below 2 km in order to provide finer detail of the atmospheric layer sampled by the lidar.

2.4 Results and discussion

We focus our analysis on a comparison of boundary layer evolution around the solar eclipse and around the morning and evening transitions on the same day. In this section, we divide the observations from 21 August into five periods: 1) the morning transition, 2) the first half of the eclipse (first contact to maximum eclipse), 3) the second half of the eclipse (maximum eclipse to final contact), 4) the late afternoon hours post-eclipse, and 5) the evening transition.

2.4.1 Morning transition

Figure 2.5 shows observations collected at the main tower on 21 August. A stable layer was present at the surface during the early morning hours. At 06:00 EDT, temperatures were 19.9 C at 2 m and 20.7 C at 10 m. Sunrise occurred at 07:01 EDT, and 2 m temperature exceeded 10 m temperature 29 min later at 07:30, indicating the presence of an unstable layer at the surface. Temperature throughout the morning hours rose steadily at $\sim$1.5 C hr^{-1}. Increases in H and TKE coincided with an increased vertical wind speed near the surface in the lidar measurements (Figure 2.6a). The change in sign of H also corresponded to the reversal of the temperature gradient at the main tower.

Before sunrise, winds at the main tower were from the downvalley (northwesterly) direction, with some rotations between westerly and northerly winds (Figure 2.5). These rotations can be explained by interactions between downvalley winds and westerly downslope winds from the valley sidewall. Previous studies have observed pulsating downslope winds with periods of $\sim$1 hr (e.g. Van Gorsel 2003; Kühnlein et al. 2013). A strong downslope pulse at the site

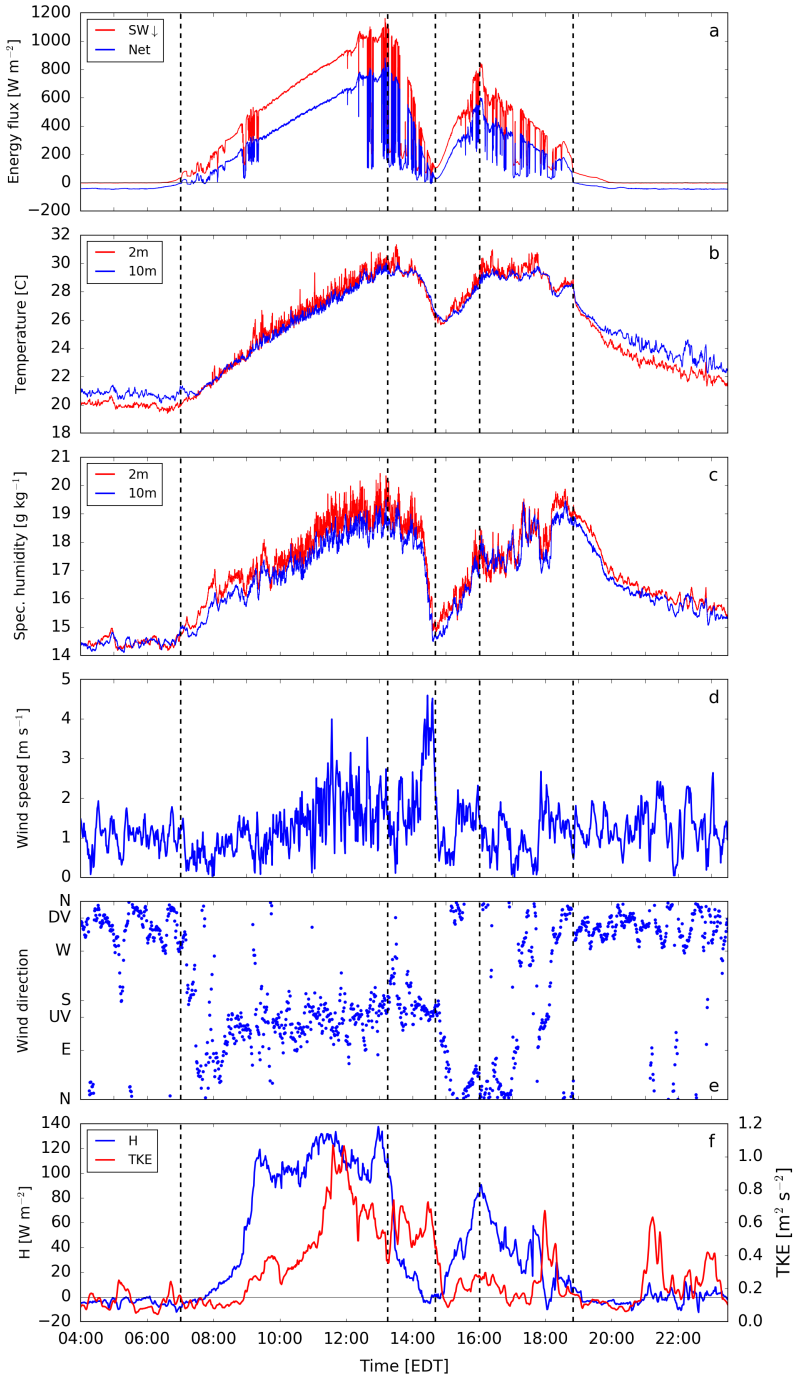

Figure 2.5: a) Incoming radiation, b) temperature, c) specific humidity, d) wind speed, e) wind direction, and f) sensible heat flux H and turbulent kinetic energy (TKE) collected at the main tower from 04:00 to 23:30 EDT on 21 August. Panels a, b, and c display raw 0.2 Hz data, while panels d and e display 1 min block averages of the 20 Hz sonic anemometer data (see Section 2.3.1). In panel f, H and TKE are shown every minute, with each point representing a 30 min average that is centered on the observation. The five dashed black lines denote sunrise, first contact, maximum eclipse, final contact, and sunset, respectively.

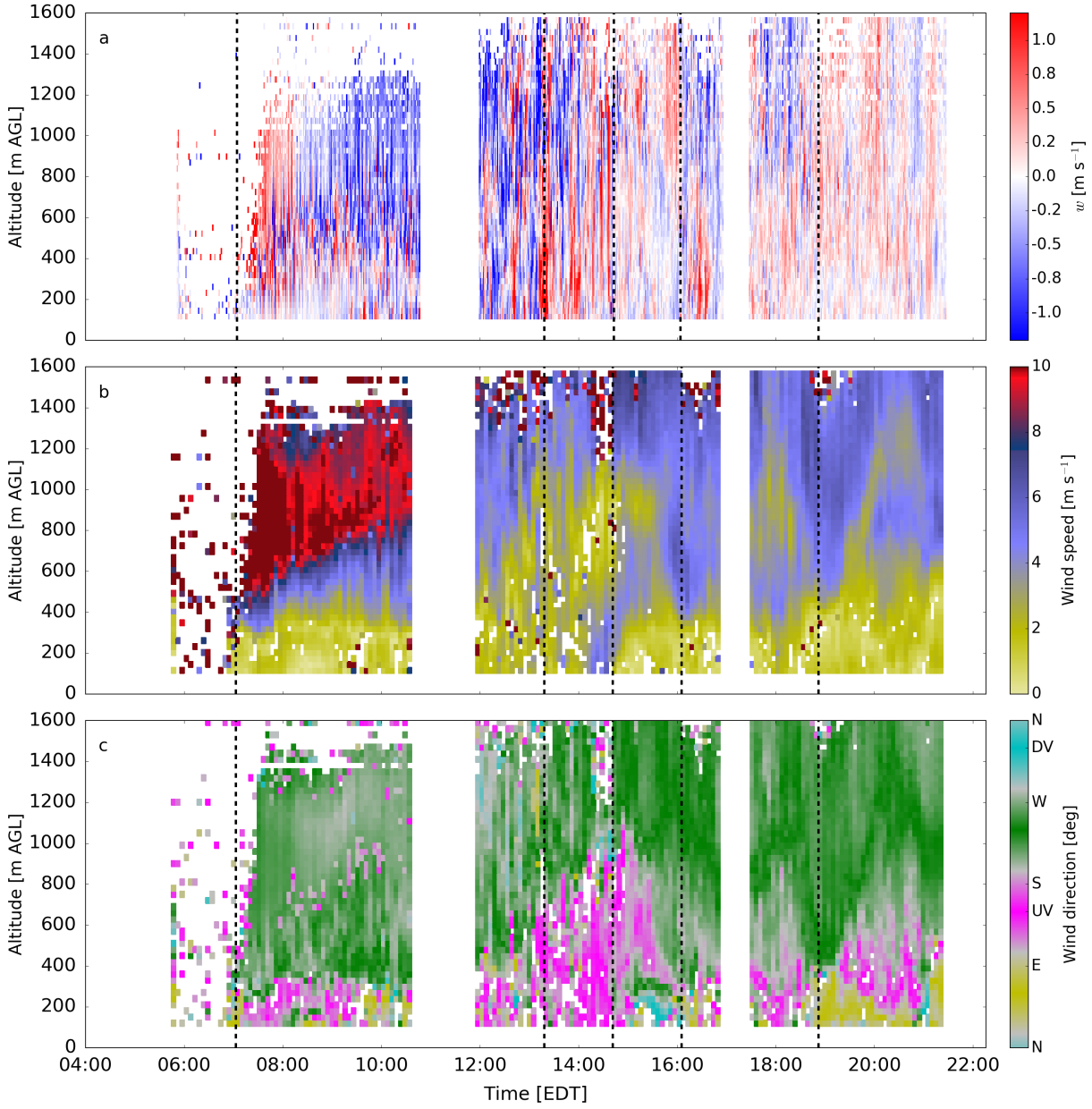

Figure 2.6: a) Vertical wind speed, b) horizontal wind speed, and c) horizontal wind direction derived from lidar observations from 04:00 to 22:30 EDT on 21 August. White squares mark missing data or periods of power outage. Dashed black lines as in Figure 2.5.

would tend to rotate nighttime winds counterclockwise (CCW) towards the west, followed by a clockwise (CW) rotation back to downvalley after the pulse subsides. Starting nine minutes after sunrise, winds at the main tower rotated CCW from downvalley to northeasterly between 07:10-07:33 EDT. Over the next 90 minutes from 07:33-09:00 EDT, a CW rotation occurred from northeasterly to upvalley winds.

Wind rotations were also recorded by all AWS during the morning transition (Figure 2.7). However, there was some variation in rotational direction between the five stations. AWS1 and AWS3 observed CCW rotations toward upvalley, while AWS5 and AWS6 observed CW rotations. AWS2 observed a pattern similar to the one observed at main tower, with winds rotating CCW from downvalley to northeasterly, then rotating CW to upvalley. By the late morning hours, the main tower and all AWS recorded steady upvalley winds.

The transition to upvalley winds in the morning is also visible in the lidar observations (Figure 2.6b, c). Winds in the first 300 m of the boundary layer were upvalley beginning shortly after sunrise, and remained fairly calm at <3 m s^{-1} throughout the morning hours. Westerly winds above this upvalley layer were due to the synoptic conditions in the region.

2.4.2 First contact - maximum eclipse (13:14-14:41 EDT)

First contact occurred in the early afternoon hours (13:14 EDT) during the presence of a convective boundary layer (CBL). Satellite imagery around this time (not shown) show convective clouds over much of the southern Appalachian Mountains, an indication that thermally-driven upslope and upvalley flows were well-developed over a large area. The main tower (Figure 2.5) and the five AWS (Figure 2.7) observed upvalley flows at first contact, with speeds around 2 m s^{-1}. Temperature and specific humidity both decreased with height at the main tower. Vertical temperature profiles collected by tethered balloon soundings show an unstable layer at the surface, with upvalley winds of 1-3 m s^{-1} throughout the layer (Figure 2.9, profile 2). Lidar observations show that the layer of upvalley winds

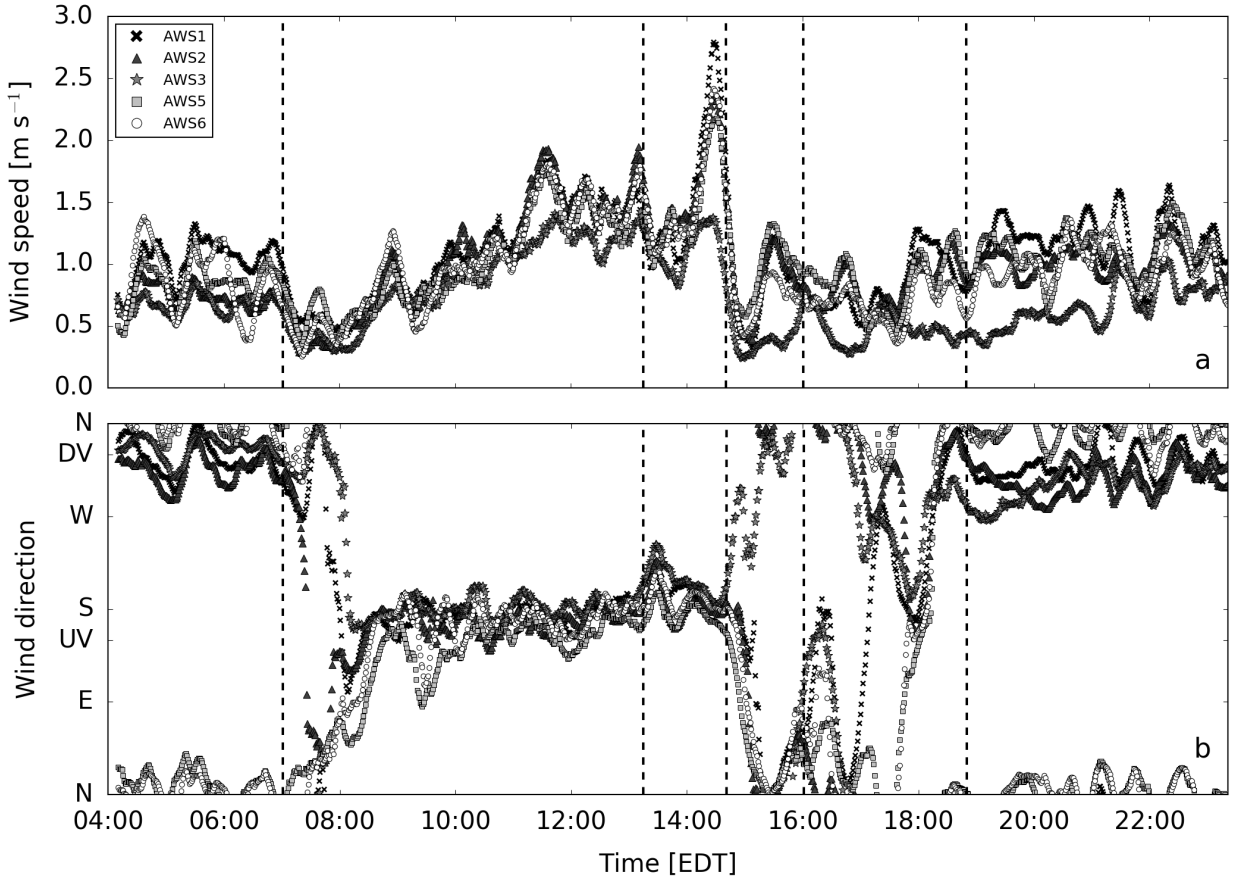

Figure 2.7: a) Wind speed and b) wind direction from all AWS from 04:00-23:30 EDT on 21 August. Each one-minute data point displayed in the two panels is a 20-minute average that is centered on the observation. Locations of the individual stations are labeled in Figure 2.1. Dashed black lines as in Figure 2.5.

had grown to a depth of 700-800 m AGL, just above height of the adjacent ridgetops (Figure 2.6). Large and fluctuating values of vertical velocity indicate vigorous turbulence in this layer. The radiosounding from 13:16 EDT shows an unstable layer beginning at the surface with a boundary layer height of approximately 1900 m AGL (Figure 2.8).

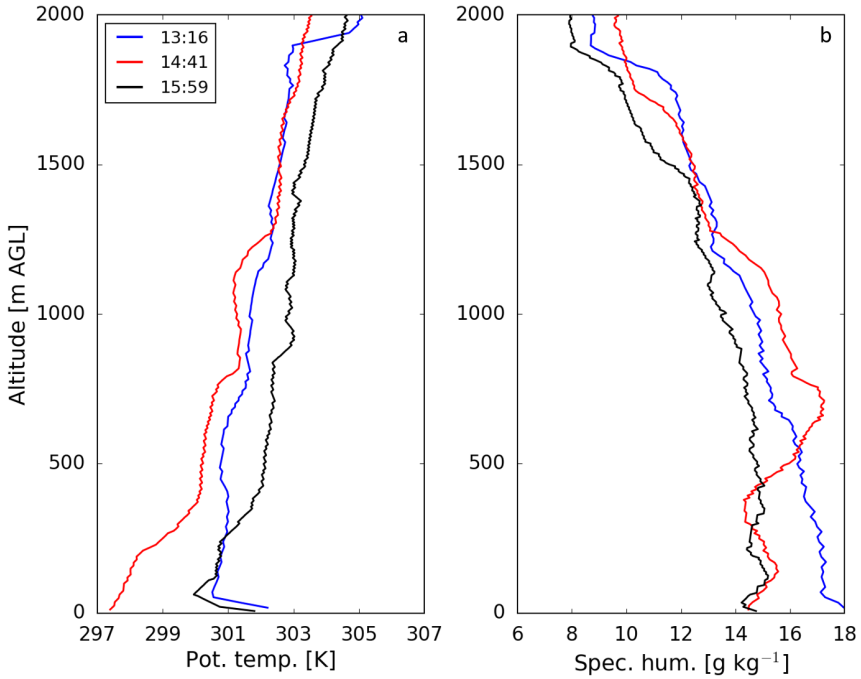

Figure 2.8: Vertical profiles of a) potential temperature and b) specific humidity from three Graw DFM-09 radiosondes launched during the eclipse. Launch times were at 13:16 (blue line), 14:41 (red line), and 15:59 EDT (black line).

Maximum eclipse occurred at 14:41 EDT. In the 87 minutes between first contact and maximum eclipse, a stable boundary layer began to form at the surface. Incoming shortwave radiation decreased to a minimum of 105 W m^{-2} at maximum eclipse (Figure 2.5). Cloud cover dissipated completely at 14:40 EDT. Temperature decreased following the decrease of incoming radiation. The vertical temperature gradient at the main tower reversed at 14:06 EDT, corresponding closely with a change from positive to negative H. Specific humidity also decreased during the first half of the eclipse, with a sharp drop between 14:15 and 14:40 EDT. Tethered balloon profiles show cooling throughout the first 100 m AGL, with a surface-based stable layer fully established in profile 6 (Figure 2.9). Above this devel-

oping stable layer was an elevated residual layer of the pre-eclipse CBL. Lidar measurements of vertical wind speed (Figure 2.6a) still show upward motions (indicating the presence of convection) above 100 m AGL from 13:14-14:41 EDT, with velocity magnitudes decreasing slightly throughout this period.

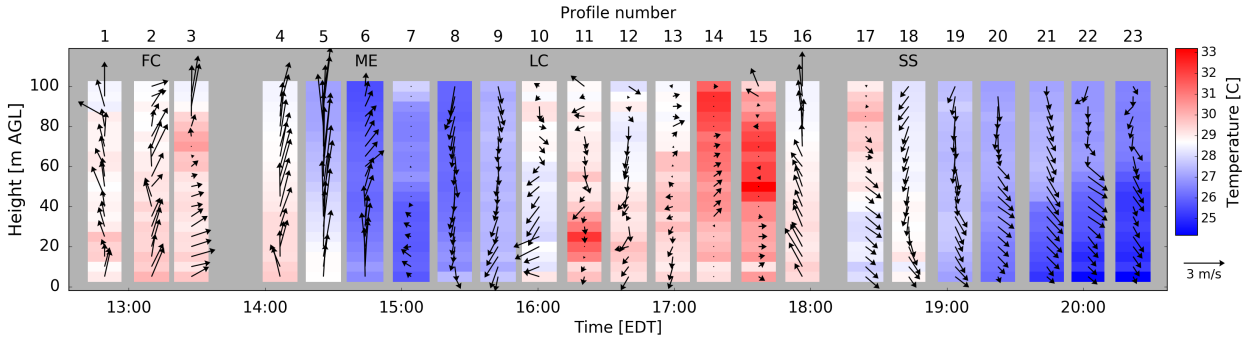

Figure 2.9: Vertical profiles of temperature (shading) and horizontal winds (vectors) collected by the tethered balloon on 21 August. The first profile begins at 12:42 EDT and the final profile begins at 20:14. Ascent rate of the balloon was 10 m every 90 s. Temperature and wind data collected by the Kestrel 4500 were bin-averaged every 5 m for this figure. FC, ME, LC, and SS denote the profiles where first contact, maximum eclipse, last contact, and sunset took place. The orientation of the wind vectors is such that a vector pointing to the top of the page indicates a southerly wind.

Winds at the main tower remained generally upvalley throughout the first half of the eclipse, with a brief rotation towards westerly between 13:20-13:40 EDT (Figure 2.5). Similar westerly shifts were recorded at all AWS and the tethered balloon during this time (Figures 2.7 and 2.9). Wind speeds increased between 14:15-14:40 EDT, with sustained wind speeds at the main tower of 3.5 m s^{-1} peaking at 4.6 m s^{-1}, the strongest 10-m winds recorded throughout the day. The timing of the wind speed increase corresponds with the sharp drop in specific humidity. This wind speed increase also appears in four of the five AWS, and in the lidar data beginning at 14:15 EDT (Figure 2.6b). Wind speeds of about 4 m s^{-1} were first observed at the lowest vertical levels (100-150 m AGL), then propagated vertically to a height of 500-900 m AGL over ∼30 min.

2.4.3 Maximum eclipse - final contact (14:41-16:01 EDT)

Incoming radiation rose steadily from 105 W m^{-2} at maximum eclipse to ∼700 W m^{-2} at final contact (16:01 EDT) (Figure 2.5). Convective cloud cover returned at 15:27 EDT, 46 minutes after maximum eclipse. A time lag between radiation changes and temperature response is visible in the main tower observations. The minimum temperature of 25.6 C (25.9 C) at 2 m (10 m) occurred at 14:51 (14:55) EDT, 10 (14) minutes after maximum eclipse. Temperature at 2 m (10 m) dropped a total of 5.0 C (3.7 C) during the eclipse. This decrease is relatively large compared to cooling during other eclipse events. Eugster et al. (2017) compiled 130 historical observations of air temperature during solar eclipses dating back to 1834. The majority of these observations were taken within the paths of totality of total solar eclipses. Including the results of the 190 surface weather stations from their study, the average temperature decrease due to a solar eclipse was 1.9 ± 1.4 C. The 5.0 C decrease at 2 m during the partial eclipse at our investigation area is more than two standard deviations larger than average. We note that this average value is based both partial and total solar eclipse events that occurred at various times throughout the day. Eugster et al. (2017) reported that the temperature reduction showed no dependence on a number of factors, including eclipse type (partial vs. total) and geographic location.

The radiosonde launched at 14:41 EDT shows that significant cooling occurred during the first half of the eclipse from the surface to approximately 800 m AGL (Figure 2.8). A stable surface layer is visible in this potential temperature profile, confirming the observations from the tethered balloon temperature profiles. The cooling both in this layer and at the surface was likely enhanced by factors other than the decrease in solar radiation, including cold air advection associated with the wind speed increase recorded at the main tower between 14:15-14:40 EDT. We hypothesize that this increase was related to a gust front caused by the downdraft from convective cells 15 km south of the investigation area (Figure 2.4). The air associated with this gust front, cooled by strong evaporation during the downdraft,

undercut the relatively warm and humid air at the investigation area. This caused additional cooling during the eclipse, as well as the sharp drop in specific humidity between 14:15 and 14:40 EDT. As the gust front passed over the investigation area, the vertical cross-section of the front became thicker (see Browning et al. 1976, Figure 3). This passage can be seen in the lidar measurements as the gust propagating vertically between between 14:40-15:00 EDT (Figure 2.6b).

The vertical temperature gradient at the main tower reversed at 15:00 EDT, 19 min after maximum eclipse. As during the morning transition, this reversal corresponded closely to the time H changed from negative to positive. The reversal indicates that a second CBL formed after maximum eclipse, breaking up the stable boundary layer that formed during the first half. Tethered balloon profiles 7-9 (Figure 2.9) show a mostly stable boundary layer, but surface warming is visible by Profile 10, which began shortly before final contact. Warming is also apparent throughout the lower atmosphere in the final radiosounding, which was launched at 15:59 EDT. Increasing solar radiation caused near-surface temperatures to almost reach pre-eclipse values. This sensible heat flux convergence contributed to local heating near the surface, but was not sufficient to account for the entirety of heating that occurred in the boundary layer during the second half of the eclipse. We hypothesize that warm-air advection contributed to the warming of the layer between 50-1000 m AGL. Surface weather stations west of the Blue Ridge Mountains (not shown) indicated temperatures that were 1-2 C warmer than at the investigation area at the time of first contact. During the second half of the eclipse, as the layer of upvalley winds eroded and westerly synoptic winds became the dominant flow above the investigation area (Figure 2.6c), the relatively warm boundary layer air west of the Blue Ridge was transported over the mountains and influenced temperature at and above the investigation area.

Almost immediately after maximum eclipse, winds in the valley began to shift. At the main tower, the sustained increase in wind speed that began at 14:15 EDT subsided at the exact

moment of maximum eclipse, accompanied by a sharp decrease in TKE (Figure 2.5). Winds rotated CCW from southeasterly upvalley flow at 14:41 EDT to a north-northeasterly flow by 15:34 EDT, 27 minutes before final contact. Winds at all AWS also shifted from upvalley to northeasterly, but the direction of rotation varied between the different stations. We provide an explanation for this variation in rotational direction in Section 2.5.

Tethered balloon profiles show that these wind rotations were not confined to the surface layer. In profiles 6-8 (Figure 2.9), winds were rotating CCW from upvalley to downvalley. In profiles 9 and 10, winds at the surface were northeasterly, while winds in the upper half of the column were northerly or northwesterly. Lidar observations show the formation of a downvalley wind layer up to ∼300 m AGL beginning around 15:00 EDT (Figure 2.6c). Winds in this layer were initially northwesterly, rotating northerly by final contact. Winds in the layer from 300-1000 m AGL began as upvalley during this period, then rotated CW and were southwesterly at final contact.

2.4.4 Late afternoon hours, post-eclipse (16:01-18:00 EDT)

After final contact, the CBL continued to develop as incoming radiation returned to normal afternoon levels and temperature increased in the CBL (Figure 2.9, profiles 11-13). Strong vertical motions returned near the surface (Figure 2.6a), but were not re-established above an altitude of 600 m AGL. Hence, although the increased radiation after 14:41 EDT was enough to break up the surface stable layer that formed during the eclipse, it was not enough for the CBL to attain a depth typical of a warm summer day.

Winds in the valley shifted multiple times after final contact. At the main tower (Figure 2.5), north-northeasterly winds that established at 15:34 EDT persisted until 17:00, then rotated CCW to westerly winds between 17:00 and 17:11. This CCW rotation was in the opposite direction of the CW rotation during the second half of the eclipse. After this brief period, an abrupt shift to upvalley winds occurred between 17:44 and 17:49 EDT, accompanied by

an increase in TKE. Upvalley winds remained until 18:00 EDT.

The five AWS also recorded multiple rotations in surface winds in the late afternoon hours (Figure 2.7). Again the direction of rotation varied between the stations. AWS1 recorded wind rotations similar to those at the main tower (AWS1 was also the closest station to the main tower). During this same period, the rotations recorded at AWS5 and AWS6 show close agreement, but the rotations at these stations differed in timing and rotational direction from those at the main tower. Additionally, AWS2 and AWS3 recorded wind rotations that were different from those recorded at either the main tower or at AWS5 and AWS6. By 17:50 EDT, winds at all AWS had changed to upvalley.

Measurements in the lower atmosphere also show a period of transitional winds after final contact. Winds were light with highly variable direction during profiles 11-15 recorded by the tethered balloon (Figure 2.9). In Profile 16, the final profile of the late afternoon hours, southeasterly upvalley winds were re-established below 60 m AGL. The downvalley wind layer visible in the lidar observations continued to rotate CW after final contact, with northeasterly winds between 16:05-17:00 EDT (Figure 2.6c). A gap in the data exists between 17:00-17:40 EDT. When observations came back online at 17:40 EDT, winds above the valley floor had changed back to upvalley up to a height of 400 m AGL.

2.4.5 Evening transition

Local sunset, i.e. the time the sun set behind the valley sidewall, was at 18:50 EDT. Incoming radiation decreased 44 W m^{-2} between 18:49 and 18:50 EDT (Figure 2.5) and then decreased more slowly until 19:57 (astronomical sunset). Temperature at 2 m dropped a total of 5.0 C during the eclipse, reaching its minimum value 97 minutes after first contact. In the 97 minutes after sunset, 2 m temperature fell from 29.0 C to 23.5 C, for a total of 5.5 C. The total temperature decrease was similar during the two periods, but the cooling rate patterns differed. During the eclipse, temperature decrease followed a quasi-sinusoidal

pattern, with a maximum cooling rate of 4.5 C hr^{-1} around 14:20 EDT. In contrast, the evening transition decrease followed an exponential pattern with a much stronger initial cooling rate of 1.0 C min^{-1}, which quickly tapered to approximately 3 C hr^{-1}.

Although the initial temperature drop during the evening transition coincided with the local sunset at 18:50 EDT, winds in the valley shifted 30 minutes earlier. A CW rotation occurred from upvalley to downvalley at the main tower between 18:10 and 18:20 EDT (Figure 2.5). H at the tower decreased fairly steadily throughout the late afternoon hours. By the time downvalley winds began at 18:20 EDT, H was less than 10 W m^{-2}. Similarly, small values of H between 18:00-18:41 precede the CW rotation from upvalley to northeasterly winds at the main tower. However, wind shift during the eclipse occurred only ∼90 minutes after temperature began to decrease, as opposed to 30 minutes before the temperature decrease during the evening transition. Wind changes therefore appear to be sensitive to sign changes in net radiation received at the surface, consistent with previous studies (Whiteman et al. 1989, 1999).

Several variables responded to the solar eclipse in a way that could be expected from previous studies. For example, the reduction in incoming radiation caused H and air temperature to decrease. The similar response of specific humidity suggests that latent heat flux decreased alongside sensible heat flux. Shifts in wind direction were expected in the context of upvalley and downvalley winds, but the variation in the CW/CCW rotational direction at different locations in the investigation area was unexpected and warrants further investigation.

2.5 Wind rotation hypothesis and conceptual diagram

Wind direction measurements at multiple locations in the investigation area give an idea of the complex terrain-wind interactions in this section of the valley. Our instrumented valley floor in particular appeared to be a suitable area for the investigation of the convergence be-

tween downslope winds and downvalley winds. We hypothesize that although the conditions created by the solar eclipse were analogous to the morning and evening transitions, wind patterns were different due to the higher solar angle during the solar eclipse. Figure 2.10 is a conceptual diagram of the convergence between downslope and downvalley winds, which is described in more detail below.

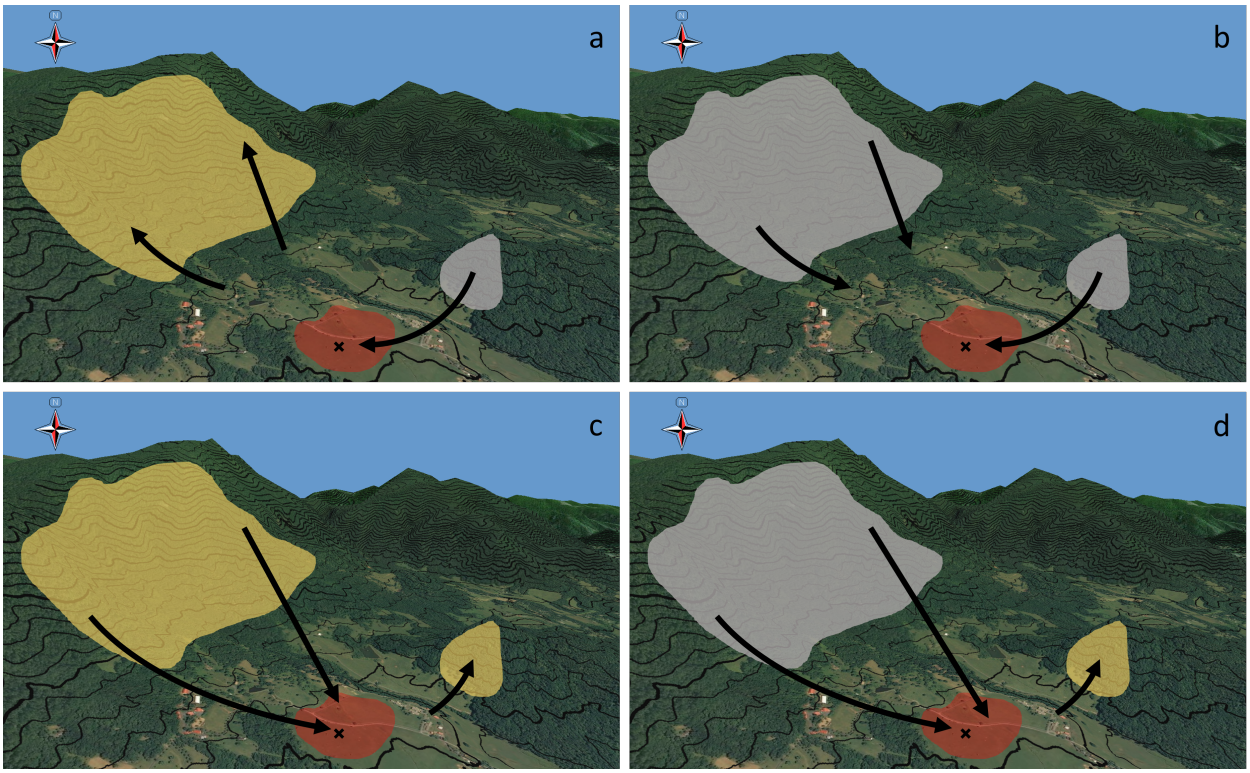

Figure 2.10: Conceptual diagram of the terrain-wind interactions at the investigation area. Slopes are either in direct sun (yellow shading) or shaded (gray shading). The wind convergence zone on the valley floor is shaded red, with the black X marking the approximate location of the main tower. Arrows denote the general direction of slope flows over the two terrain features. Contour interval is 20 m. The four panels show the conditions during a) the morning transition, b) the first half of the eclipse, c) the second half of the eclipse, and d) the evening transition. See Section 2.5 for additional discussion.

During a typical evening transition in this valley, the last rays of the afternoon sun are incident upon the southwestern face of the small hill to the northeast of our investigation area. Meanwhile, the valley sidewall to the west has been shaded for some time. Therefore, downslope winds develop earlier over the sidewall than over the hill. These westerly sidewall downslope winds (see Figure 2.2) flow into the convergence zone at the valley floor and cause

a CW rotation away from the southeasterly upvalley winds. This transition is apparent in the wind observations at all AWS between 18:00 and 18:10 EDT (Figure 2.7) and at the main tower between 18:10 and 18:20 EDT (Figure 2.5). The rotation stops as northwesterly downvalley wind becomes the dominant flow in the investigation area.

A short time later, downslope winds start over the slopes of the small hill. The resulting northeasterly hill downslope winds enter the convergence zone, but are not as pronounced as the westerly sidewall downslope winds. As a result, the hill downslope winds are only able to weakly penetrate the convergence zone. The northeasterly influence is most apparent at AWS5 and AWS6 before 08:00 EDT and after 19:00 EDT (Figure 2.7). These two stations are the closest in proximity to the hill. Microterrain features at the investigation area (Figure 2.1), including a small gully between AWS2 and the main tower, also prevent the hill downslope winds from penetrating further into the convergence zone. Small CW and CCW rotations throughout the night recorded by the main tower and all AWS are a result of intermittent downslope flows from the two terrain features. A brief, strong pulse of downslope winds from the hill would cause a CW rotation, while a pulse from the sidewall would cause a CCW rotation.

Cooling over the two terrain features happened in a different way during the first half of the eclipse. The solar altitude angle was much higher in the early afternoon hours than during the evening transition, and the solar azimuth angle was much smaller (i.e. closer to south than to west). Due to these different angles, incoming radiation was similar on both the hill and the sidewall at the time of first contact. Hence, as radiation levels decreased during the first half of the eclipse, the atmosphere over both terrain features cooled at the same time. The northeasterly hill downslope winds were the first to develop and enter the convergence zone. This caused the CW rotation observed shortly after maximum eclipse at the main tower (Figure 2.5) and four of the five AWS (Figure 2.7). The rotation was recorded several minutes earlier at AWS5, AWS6, and AWS2 than at the main tower. In addition to the

closer proximity of these three AWS to the hill, the small gully separating the main tower from the AWS slightly delayed the arrival of the hill downslope winds at the main tower. AWS3 was the only station that did not observe a CW rotation during the second half of the eclipse. We hypothesize that the microterrain features in the convergence zone prevented the hill downslope winds from reaching that station (Figure 2.1).

The second half of the eclipse shares some similarities with the morning transition. In a typical morning transition at our investigation area, the eastern face of the valley sidewall is heated for several hours after sunrise before the southwestern face of the hill receives any direct radiation. Therefore, upslope winds start over the sidewall before they form over the hill, allowing northeasterly downslope winds from the hill slopes to penetrate further into the convergence zone. These features result in a CCW rotation from northwesterly downvalley winds to northeasterly winds at the main tower between 07:05 and 07:30 EDT (Figure 2.5). As incoming radiation increases throughout the morning, upvalley winds develop and become the dominant flow in the investigation area. This explains the CW wind rotation from northeasterly to upvalley winds observed at the main tower between 08:00 and 09:30 EDT.

Further evidence for this interaction between slope and valley winds is provided by the AWS observations (Figure 2.7). As sidewall downslope winds weakened and reversed to upslope winds, AWS5 (the station nearest the hill; see Figure 2.1) recorded winds steadily from the northeast between 07:12 and 07:46 EDT. These northeasterly winds soon reached other nearby stations. Northeasterly winds were recorded at AWS6 beginning at 07:30 EDT, and at AWS2 beginning at 07:40 EDT. At 08:00 EDT, wind direction at these three stations began to rotate CW with the onset of upvalley winds. As upvalley winds strengthened, a CCW rotation from downvalley to upvalley winds occurred at AWS1 between 07:45 and 08:10 EDT and at AWS3 between 08:01 and 08:15. Strengthening upvalley winds prevented the northeasterly winds from the hill from reaching AWS1 and AWS3, resulting in a CW rotation at those stations. Winds at all five AWS were upvalley by 08:40 EDT.

Heating of the sidewall and hill slopes occurred differently in the second half of the eclipse compared to the morning transition. As incoming radiation steadily increased after maximum eclipse, the hill and sidewall were heated simultaneously. Winds over the hill again responded more quickly than winds over the sidewall due to the relative size of the two terrain features. The weakening of the hill downslope winds allowed sidewall downslope winds to penetrate further into the convergence zone. The main tower observed these westerly sidewall downslope winds between 17:11 and 17:44 EDT (Figure 2.5).

Sidewall downslope winds caused CCW rotations toward westerly winds at AWS3 between 16:42 and 16:56 EDT and at AWS2 between 16:54 and 17:09 (Figure 2.7). AWS5 and AWS6 recorded smaller CCW rotations during this time. Northeasterly hill downslope winds were still dominant at AWS5 and AWS6, which prevented a larger CCW rotation to fully westerly winds. We hypothesize that the CW shift to westerly winds observed at AWS1 between 16:52 and 17:21 is the result of interactions between weakening hill downslope winds, strengthening upvalley winds, and sidewall downslope winds reaching that station. In the 30 minutes before sunset, all AWS recorded a rotation to upvalley winds. The direction of this rotation varied depending on the location of the stations relative to the two terrain features. Wind direction at AWS1, AWS2, and AWS3 was mainly influenced by sidewall downslope winds, and the rotation at these stations was CCW from northwesterly to southeasterly. Weakened hill downslope winds were still present at AWS5 and AWS6, and the rotation at these stations was CW from northeasterly to southeasterly.

The interaction between the phases of the slope and valley wind systems causes a daily wind direction rotation on the valley sidewalls (Hawkes 1947; Whiteman 2000). Previous studies of wind rotations in valleys have focused mainly on sidewall sites (Whiteman et al. 1989; Li and Atkinson 1999; Whiteman et al. 1999), and Eugster et al. (2017) noted wind rotations at several stations situated on valley sidewalls during the 20 March 2015 solar eclipse. The observations from 21 August in the present study indicate that the explanation of the nature

of rotations over these sidewalls can be extended to locations at and above the valley floor. The magnitude and direction of rotation at various locations over the valley floor appears to vary between the morning and evening transitions, and is also dependent on local terrain features. These rotations can impact e.g. the dispersion of air pollutants from emission sources in different parts of the valley, and therefore can have important implications for air quality studies.

2.6 Summary, conclusions, and future work

The focus of this study was the observation of thermally-driven orographic winds during the 21 August 2017 solar eclipse. We observed these winds in a small valley to determine if eclipse-induced changes in radiation and temperature are sufficient to disrupt the normal diurnal cycle of slope and valley winds. Our analysis of the observations provided the following results:

- Surface cooling was more than two standard deviations larger than average compared to previous solar eclipse events. This cooling in the presence of negative daytime sensible heat flux caused the formation of a stable layer at the surface.
- Vertical temperature profiles from tethered balloons and radiosondes indicate that cooling during the first half of the eclipse extended to 800 m AGL, and warming during the second half extended above 2000 m AGL. The daytime sensible heat flux was not sufficient to explain these temperature changes, and advection played a role in the cooling and warming of the lower atmosphere.
- Surface weather stations recorded multiple rotations in wind direction during and after the eclipse. These rotations can be explained by the interaction between slope and valley flows. The size and direction of the rotations were strongly influenced by the proximity of the stations to local terrain features.

- Tethered balloon and lidar observations showed that wind shifts and rotations were not limited to the surface. A layer of downvalley winds formed between the surface and ∼300 m AGL during the second half of the eclipse. Winds above this layer remained upvalley or westerly. The timing of this wind layering indicates a time lag between decreased radiation during the eclipse and the reversal of the horizontal temperature gradient. Downvalley wind was not initiated until ∼80 minutes after the start of the eclipse, and appeared in the ABL after convection was re-initiated at the surface. The downvalley wind layer existed for ∼70 minutes and dissipated shortly after final contact.

We conclude that the decreased radiation and associated cooling during the solar eclipse altered the normal cycle of thermally-driven winds in the valley. With regard to incoming solar radiation, the first and second halves of the eclipse are similar to the evening and morning transitions, respectively, but with important differences caused by the orientation of the topographic features relative to the position of the sun. The high solar elevation angle and low azimuth angle during the eclipse caused different slope heating and cooling patterns to develop than what would typically be expected during the transition periods. This different heating and cooling resulted in the varying wind patterns during the eclipse. Northeasterly downslope winds from a small hill, normally overpowered at night by downvalley flows, were able to penetrate into our investigation area during the eclipse. A conceptual diagram of these wind patterns is shown in Figure 2.10.

This study focused on the observations collected only on the day of the eclipse. We were fortunate that calm synoptic conditions prevailed at the investigation area on 21 August, and that the thunderstorm system south of the site did not disrupt our measurement campaign. The five AWS were installed at the site 60 days before the solar eclipse event. Future work will include an analysis of AWS data over this 60 day period, and one year of data from the main tower. We will characterize 'typical' wind and temperature changes during morning

and evening transitions at our site, and interpret the deviation of the wind patterns during the solar eclipse in more detail. We will pay special attention to the climatology of wind rotations on the valley floor.

Acknowledgements

We gratefully acknowledge Nich Traverse for providing access to Innisfree Farm to collect our observations. We also thank Asad Ali, Jenna Mercier, Jami Orrell, Humna Sharif, and Michael Worcester for their work in the field.

Chapter 3

Contextualizing eclipse observations using a climatological analysis of meteorological data at Innisfree

3.1 Introduction

Chapter 2 presented meteorological observations made during the 21 August 2017 solar eclipse at Innisfree, a farm in a small valley near the Blue Ridge Mountains. Several meteorological variables responded to the eclipse approximately as expected based on previous studies. For example, near-surface temperatures dropped as a result of the decrease in incoming solar radiation. The decreased radiation also reduced sensible heat flux at the surface and dampened convection throughout the atmospheric boundary layer (ABL). In the second half of the eclipse, temperatures rose, sensible heat flux became more positive, and convection was initiated once again at the surface. The primary objective of these observations was to document changes in thermally-driven winds due to eclipse-induced cooling and subsequent warming. The afternoon of 21 August featured multiple wind shifts during and after

the eclipse, a direct result of the changes in incoming radiation during the eclipse. The various surface weather stations on the valley floor recorded different wind patterns that were strongly influenced by the proximity of the stations to topographic features in the valley.

One of the most interesting features in the wind observations from 21 August is the counterclockwise (CCW) rotation from southerly upvalley winds to northeasterly winds that began immediately after maximum eclipse. This event can be separated into two phases: the initial CCW rotation, followed by the period of northeasterly afternoon winds. Both features were unexpected when considering the investigation site and the surrounding valley geometry. Significant rotations in surface wind direction have been described at sites on valley sidewalls (Hawkes 1947; Whiteman 2000), but surface wind measurements during the eclipse were made at the valley floor, where such rotations are not well-documented in the literature. Wind rotations that regularly occur over valley floors could impact aerosol dispersion and air quality in a given valley. The northeasterly winds following this CCW rotation were unexpected because the valley axis at Innisfree runs northwest to southeast. With this geometry, northeasterly winds are not expected to occur during the afternoon when conditions are primarily thermally-driven.

To further investigate the significance of the wind rotation and northeasterly winds on the afternoon of 21 August, it is necessary to examine the frequency of the two features over a longer time period. To this end, this chapter considers a one-year climatological record of observations from the main tower at Innisfree. Specifically, wind direction observations are analyzed to identify persistent wind rotations and periods of northeasterly wind during thermally-driven days at Innisfree. This chapter seeks to address the following research objectives:

1. Identify thermally-driven days at Innisfree that occurred over the course of one year.
2. Compare observations collected during the eclipse to those collected during diurnal transition periods on thermally-driven days.

3. Identify synoptic weather patterns that may allow for the development of thermally-driven flows at Innisfree.

The remainder of the chapter is organized as follows: a description of the data filtering used to identify thermally-driven days is presented in Section 3.2. Analysis methods are described in Section 3.3, followed by a discussion of results in Section 3.4. A summary and conclusions are presented in Section 3.5.

3.2 Methodology: Data filtering

The main tower used in the field campaign was installed at Innisfree in August 2016. A year-long climatology from October 2016 through September 2017 provides the necessary data to determine a 'typical' diurnal cycle of thermally-driven winds at Innisfree. Some of the sensors used to make observations during the eclipse were installed in May 2017, and do not have full data coverage over this year-long period. Instruments used in the following analysis include two thermohygrometers at 2.0 and 9.4 m above ground level (AGL) mounted in naturally ventilated radiation shields; a pyranometer at 3.7 m AGL to measure incoming solar radiation; a propeller anemometer at 9.5 m AGL; and a 3-dimensional sonic anemometer at 10 m AGL. With the exception of the sonic anemometer, all instruments were set to one-second sampling with one-minute logging. The sonic anemometer recorded measurements at 20 Hz, which were processed in the manner detailed in Section 2.3.1. Wind direction from both anemometers is measured from true north.

On synoptically active days, frontal passage or forced channeling causes winds to deviate from the expected diurnal cycle of slope and valley winds. To focus on thermally-driven days, the synoptically active days must be filtered out of the climatology. This filtering process is described below. Due to some technical issues with the sonic anemometer over the course of the year, several data gaps ranging from days to weeks are present during

the climatology. Hence, for better data coverage, the propeller anemometer data were used during the filtering process.

3.2.1 First filter: visual inspection

The primary goal of the data filtering was to identify 24-hour periods where the wind patterns recorded at the main tower are indicative of thermally-driven winds. More specifically, this includes downvalley winds during nighttime hours, upvalley winds during daytime hours, transitional periods between night and day, and wind speeds that do not suggest synoptic influence. The first step in isolating thermally-driven days was to visually examine the data during the morning and evening transitional periods, which were analyzed separately for each day. Four criteria were considered:

- **Reversal in the $T_2 - T_{10}$ temperature gradient.** The formation of a stable boundary layer overnight (i.e. $T_2 < T_{10}$) is indicative of calm synoptic conditions. The reversal of this temperature gradient during the morning transition (i.e. $T_2 > T_{10}$) indicates the development of a convective boundary layer and strong radiative input at the surface. During the evening transition, T_2 falling below T_{10} indicates the formation of a new stable boundary layer at the surface.

- **Clear skies.** Because thermally-driven winds are dependent on strong incoming radiation, only days with clear or mostly clear skies were selected. Days with significant cloud cover (determined visually by discontinuities in the incoming radiation curve) were rejected.

- **Reversal in wind direction.** The specific timing of the wind reversal during the transition periods was not considered in this step. Instead, days that did not feature obvious upvalley/downvalley wind reversals around sunrise and sunset were rejected.

- **Low wind speeds.** The shift in wind direction during the morning and evening

transitions typically results in relatively low wind speeds. Days that featured sustained or increased winds during these transitions were rejected.

Figure 3.1 shows observations from two days in the year-long data set to exemplify the filtering procedure. Observations from 16 October 2016 show a few clouds in the afternoon, but the incoming radiation curve is generally quite smooth. A temperature inversion existed in the early morning hours, which was quickly broken up after sunrise. A clear shift in wind direction is visible, with upvalley winds during the day and downvalley winds at night (both before sunrise and after sunset). Low wind speeds provide additional evidence that the conditions were primarily thermally-driven. Both the morning and evening transitions on 16 October were selected to progress to the next round of filtering. The radiation curve from 21 November 2016 shows completely clear skies throughout the day, but other variables indicate that thermally-driven flows did not develop under these cloudless conditions. Temperature at the two measurement levels did not show signs of an inversion forming or breaking up, and winds blew downvalley throughout the day. High wind speeds indicate that the conditions in the valley were synoptically-driven. Both the morning and evening transitions from 21 November were rejected during this stage of filtering.

90 morning transitions and 120 evening transitions were identified as having characteristics of thermally-driven winds after the first round of filtering (Figure 3.2a, b).

3.2.2 Second filter: synoptic wind data

It is possible that conditions in a valley may indicate the presence of thermally-driven winds, when in fact there is strong synoptic influence present in the wind patterns. This would occur when the synoptic-scale wind is channeled through the valley in upvalley direction during the day and in downvalley direction at night.

North American Regional Analysis (NARR) data were used to remove this possibility from

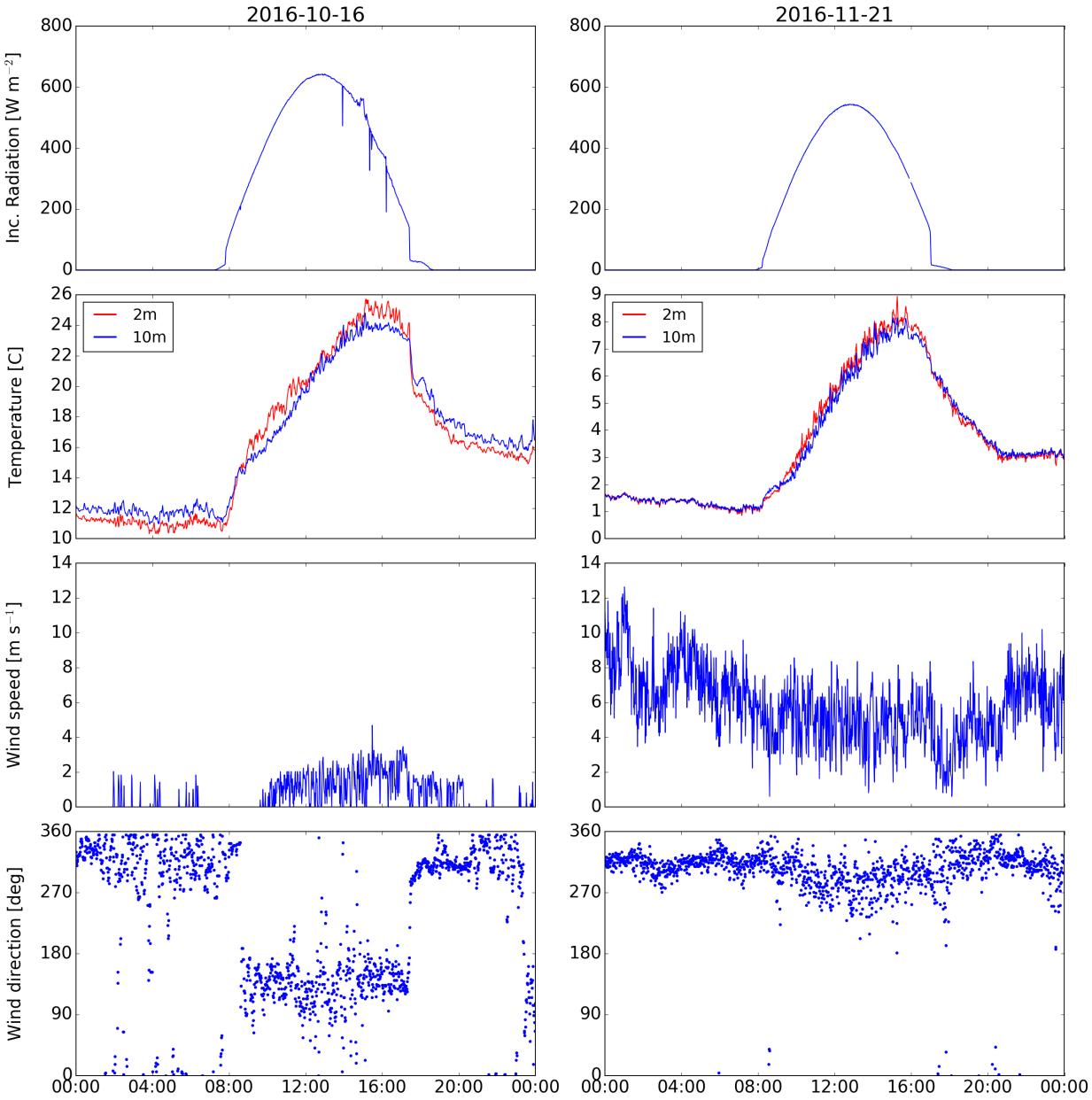

Figure 3.1: Observations of incoming radiation, temperature at 2 m and 10 m, wind speed, and wind direction from the main tower at Innisfree on 16 October 2016 (left column) and 21 November 2016 (right column).

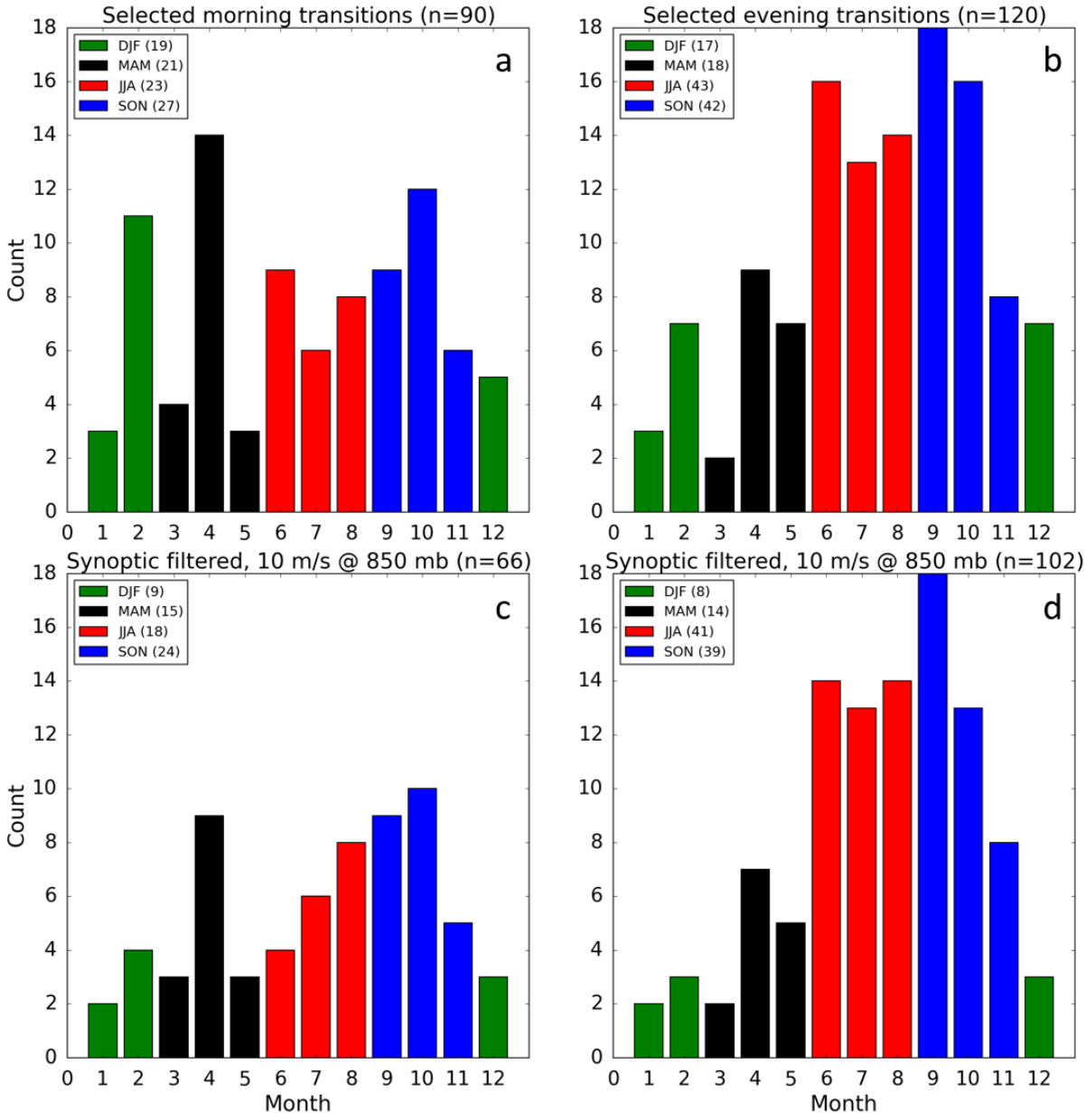

Figure 3.2: Top row: selected morning (a) and evening (b) transitions after initial visual filtering. Bars are color coded by season. Bottom row: morning (c) and evening (d) transitions remaining after filtering by 850 mb synoptic wind speed.

the selected dates after the first round of filtering. 850 mb winds were examined at 06:00, 09:00, 18:00, and 21:00 (all local time - the approximate times of the morning and evening transitions throughout the calendar year). A threshold wind speed was set at 10 m s^{-1}, and transitions selected after the first round of filtering were discarded if the NARR 850 mb wind exceeded this threshold. This resulted in the number of morning transitions decreasing from 90 to 66, and the number of evening transitions decreasing from 120 to 102 (Figure 3.2c, d).

At this point, conditions on a given day were considered to be thermally-driven if both morning and evening transitions had passed through the first two rounds of filtering. 47 days were selected at this stage of the filtering process. 21 August 2017, the day of the eclipse, was still present in the dataset at this point, indicating that conditions were thermally-driven during the eclipse event.

3.2.3 Third filter: additional visual inspection

The first two rounds of data filtering only considered the conditions around the morning and evening transitions. The eclipse day featured quasi-transitions in the middle of the afternoon. Hence, the daytime hours in the climatology are also of interest for comparison, and another round of visual filtering was applied to remove previously selected dates where synoptic influence was present in the daytime wind data. This involved removal of days where surface winds over 4 m s^{-1} sustained for longer than one hour (typical daytime wind speeds on thermally-driven days are 2-3 m s^{-1}). This final round of filtering reduced the number of selected dates from 47 to 18. Data from 21 August (the eclipse day) were removed from the dataset during this stage of filtering.

The visual data filtering described in Sections 3.2.1-3.2.3 above was completed using observations from the propeller anemometer. The sonic anemometer data are collected at a higher frequency, and are more accurate than data from the propeller anemometer, especially at low wind speeds (< 0.5 m s^{-1}). The propeller anemometer has threshold wind speeds of

0.4 m s^{-1} for the propeller and 0.5 m s^{-1} for the wind vane. Winds below these threshold speeds are not strong enough to spin the propeller or turn the vane. The sonic anemometer has no minimum wind speed threshold and has a resolution of 0.01 m s^{-1}. The main wind observations from the eclipse day under investigation are the rotations and northeasterly winds between maximum eclipse and sunset. During this period, wind speeds measured by the sonic anemometer were generally under 1 m s^{-1}, and frequently fell below 0.5 m s^{-1}. See Appendix B for a comparison of observations from the sonic and propeller anemometers.

Fifteen of the 18 dates remaining after the final round of filtering were present in the sonic anemometer dataset for the full 24-hour day. These 15 dates are the final dates selected for climatological analysis in the following sections. The 15 dates are listed in Table 3.1, and are referred to in the following text as the *filtered climatology*.

Table 3.1: List of dates in the final filtered climatology.

2016-10-15	2016-10-16	2016-10-20
2016-10-26	2016-11-07	2016-11-08
2016-11-13	2016-11-18	2017-04-09
2017-07-16	2017-07-17	2017-07-31
2017-08-03	2017-08-20	2017-09-24

3.3 Methodology: Data analysis

3.3.1 Defining wind rotations

To analyze the filtered climatology for wind rotations, it is necessary to first define such rotations. Two criteria were chosen:

- **Time threshold:** the measured wind direction must turn either clockwise or counterclockwise for a minimum of 10 consecutive observations (i.e. for 10 consecutive minutes).

- **Magnitude threshold:** For each period of consecutive rotation in the same direction for at least 10 minutes, the circular magnitude of the rotation was obtained by subtracting the first and last wind direction values of the period. Rotations were then sorted into four groups by magnitude:
  - ⋆ **< 30 degrees:** Small rotations of 30 degrees or fewer are observed regularly throughout the daytime and nighttime hours, when the dominant flow at the main tower is in the upvalley or downvalley direction. These rotations are an interesting feature of the winds at Innisfree, but are not the focus of this investigation.
  - ⋆ **$30 - 90$ degrees:** This category represents a rotation that spans over approximately one sector of the compass, e.g. from southerly to westerly winds. This is an important distinction at Innisfree for separating westerly downslope winds from northerly/northwesterly downvalley winds during evening transitions.
  - ⋆ **$90 - 135$ degrees:** The third category was chosen specifically to encompass the CCW rotation from southerly upvalley wind to northeasterly wind that occurred immediately after maximum eclipse.
  - ⋆ **> 135 degrees:** The final category represents a shift in valley winds, i.e. from upvalley to downvalley. Rotations of this magnitude are not expected to occur frequently outside of the morning and evening transition periods.

In the following discussion, rotations in the above categories are referred to as Magnitude I (smallest), Magnitude II, Magnitude III, and Magnitude IV (largest) rotations. For the discussion on the sensitivity of the wind rotation analysis to the time threshold, see Section 3.4.1.

Some additional preprocessing of the sonic anemometer directional data was necessary to identify rotations in the filtered climatology. A moving average with an 11-minute window was applied to the 1-minute block averaged data. This moving average was adjusted to

account for the discontinuity between 360 and 0 degrees. The window for the moving average considered the five minutes of wind information before and after a given timestamp. The window width chosen to remove some of the noise from the wind direction data, but still retain smaller-scale rotations like those in the first magnitude category.

Once this additional preprocessing was completed, all rotations in each of the 15 days in the filtered climatology were identified. An example is given in Figure 3.3. A total of 800 rotations were identified in the filtered climatology. After this identification, some descriptive statistical analysis can be performed to determine if rotations of a certain magnitude are likely to occur during certain times of day. This analysis is presented in Section 3.4.

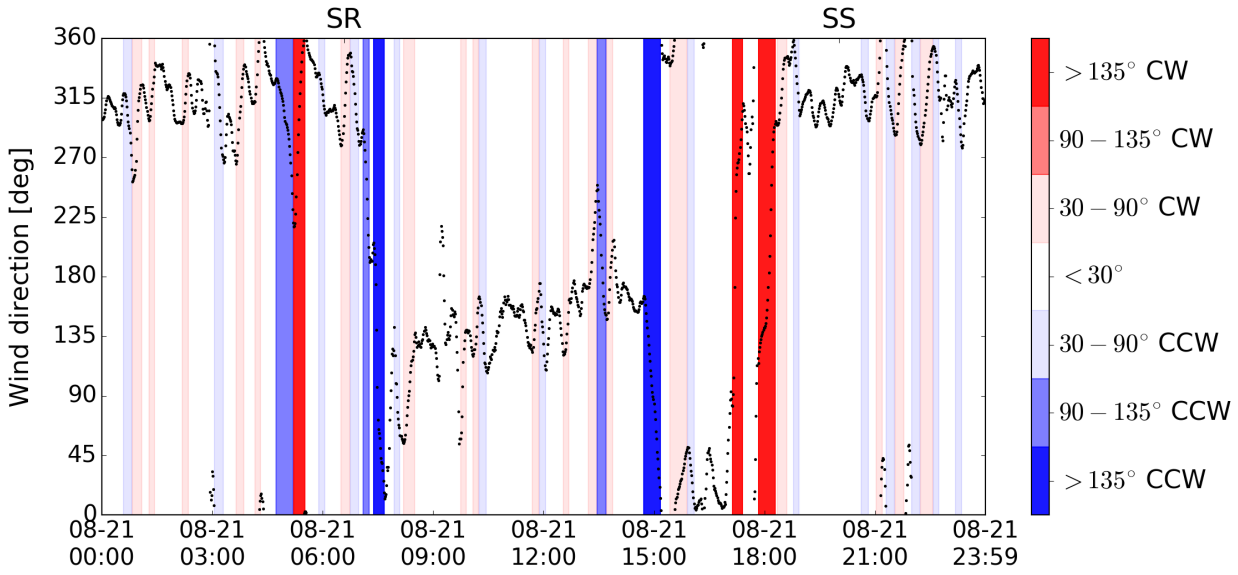

Figure 3.3: Wind direction data from 2017-08-21 (eclipse day) with CW and CCW wind rotations identified in red and blue highlighting, respectively. For clarity, rotations with magnitudes less than 30 degrees are not highlighted. Tick labels on the top axis indicate sunrise and sunset times.

3.3.2 Defining northeasterly wind

To investigate the significance of the daytime northeasterly wind on the eclipse day, observations of northeasterly wind were subset from the filtered climatology. Here northeasterly wind is defined as wind blowing from $11.25 - 78.75$ degrees. These limits were determined by

dividing the compass into 16 directional components, and constructing a quadrant from four components, e.g. N, NNE, NE, and ENE. Each of these components spans a range of 22.5 degrees, where the middle of the range contains the true cardinal direction (e.g. northerly wind blows between $348.75 - 11.25$ degrees). Hence, the definition of northeasterly wind used in the following analysis includes winds from the NNE, NE, and ENE. Unlike the rotation identification in the previous section, no minimum time threshold was used with the wind direction data.

3.4 Results

3.4.1 Rotations

Wind rotations happen at all hours of the day at Innisfree, but the focus for this analysis is the morning and evening transition periods, which occur around sunrise and sunset. Since the dates in the filtered climatology span several months, the day length varies by more than an hour between the shortest and longest days in the record. Instead of considering the hour of day in which wind rotations occur, the following analysis considers the hour relative to sunrise or sunset. A total of 800 wind rotations were identified in the filtered climatology. The distribution of rotations is fairly uniform throughout the day, with 52% occurring around sunrise and 48% around sunset. This result aligns with expectations after the visual data filtering.

Wind rotations can be further separated by the hour relative to sunrise or sunset, and by the the four magnitude categories listed in Section 3.3.1 (Figure 3.4). Each of the subplots in Figure 3.4 is normalized by the total number of rotations in the climatology (800), with no distinction made between CW and CCW rotations. In this detailed breakdown, Magnitude I and II rotations occur most frequently, representing 88% of total rotations. The frequency of Magnitude I rotations decreases in the later morning hours and increases again in the

late afternoon. This decrease may be due to the strengthening upvalley winds during these hours, which could provide a relatively steady wind direction and suppress small magnitude rotations. The continued presence of Magnitude II rotations (30-90 degrees) during these hours may be due to downmixing of ABL air toward the surface. The decrease in rotation frequency on the extreme ends of Figure 3.4a (i.e. 7-8 hours before or after sunrise) is partially a result of the latitude at the investigation area. On the summer solstice, Innisfree receives approximately 14.5 hours of daylight. Hence, for most of the days in the filtered climatology, rotations occurring more than seven hours after sunrise would register closer to sunset.

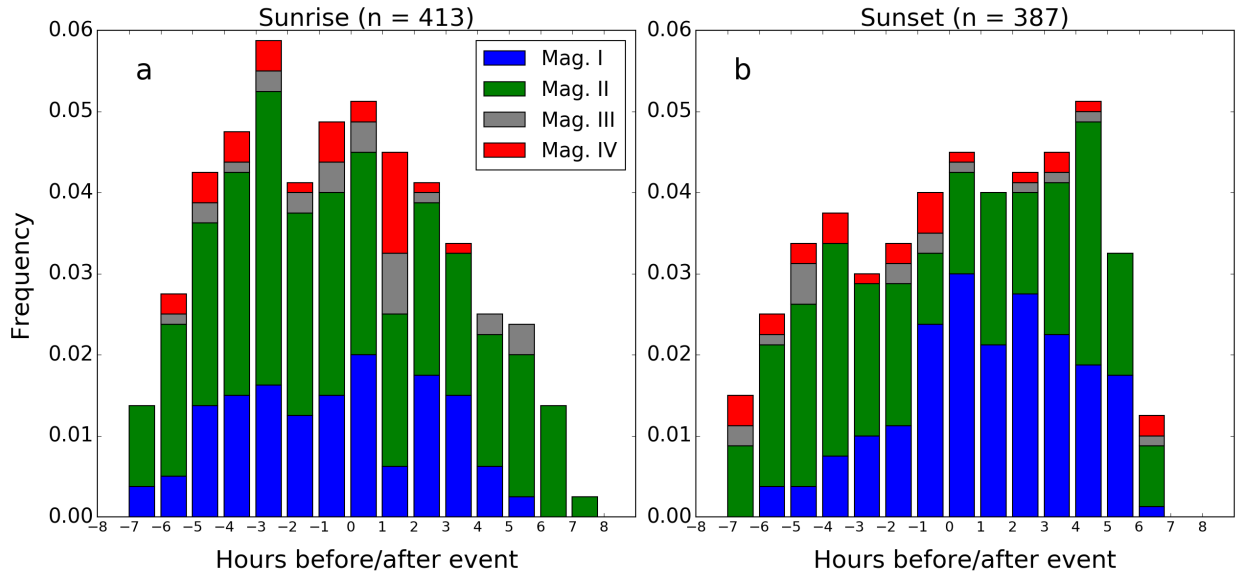

Figure 3.4: All rotations identified in the filtered climatology. Rotations that occur nearest a) sunrise and b) sunset are binned by hour relative to the sun event and colored by rotational magnitude (see Section 3.3.1).

Magnitude III and IV rotations account for only 5% and 7%, respectively, of all rotations in the filtered climatology. However, they are more pertinent than smaller magnitude rotations in the context of thermally-driven orographic winds, as they may indicate significant shifts in the wind system. For example, Magnitude IV rotations may arise as a result of winds shifting from downvalley to upvalley. An examination of Magnitude IV rotations reveals no significant preference for the rotations to occur around sunrise or sunset (Figure 3.5).

However, these large magnitude rotations that occur in the morning happen most frequently within the first hour after sunrise. Rotations in this hour range account for 33% of all Magnitude IV rotations around sunrise, and nearly 20% of overall Magnitude IV rotations. This result shows that large rotations happen primarily as a result of a reversal in valley wind direction.

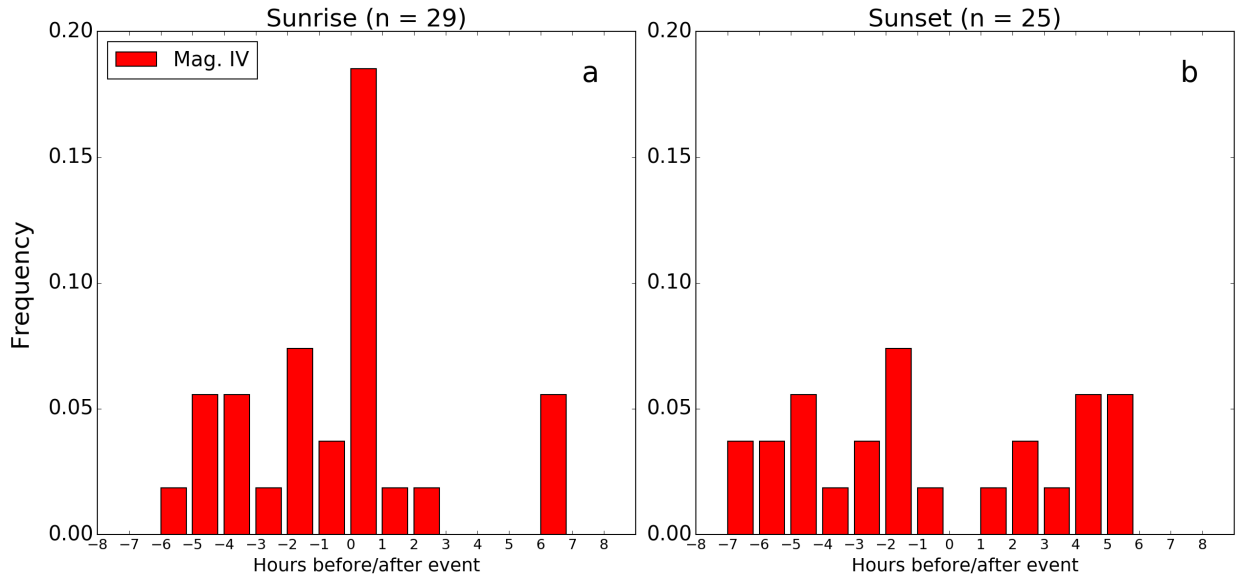

Figure 3.5: Similar to Figure 3.4, but only considering Magnitude IV rotations (red bars in Figure 3.4).

Patterns in Magnitude IV rotations become more pronounced when sorting by rotational direction (CW or CCW; Figure 3.6). Of the rotations that occur around the morning transition, 90% are in the CW direction. This result supports the hypothesis of terrain-wind interactions presented in Section 2.5. In a 'typical' morning transition, upslope winds form over the sidewall shortly after sunrise. Around the same time, northeasterly winds occur at the main tower for a brief period, rotating the mean wind clockwise from the northwest. A short time later, daytime upvalley winds dominate from the southeast. The mechanics behind this morning northeasterly flow from the hill may be different than the thermally-driven downslope winds observed during the eclipse. As the valley fills with cool air during the night, the temperature gradient that causes downslope flows around the evening transition is weakened. Hence, northeasterly morning winds may be a result of a volume of air

moving down the hill to replace the air moving up the sidewall with the onset of upslope winds. A field campaign with dense instrumentation on the hill slopes would be necessary to determine these fine details during the morning transition.

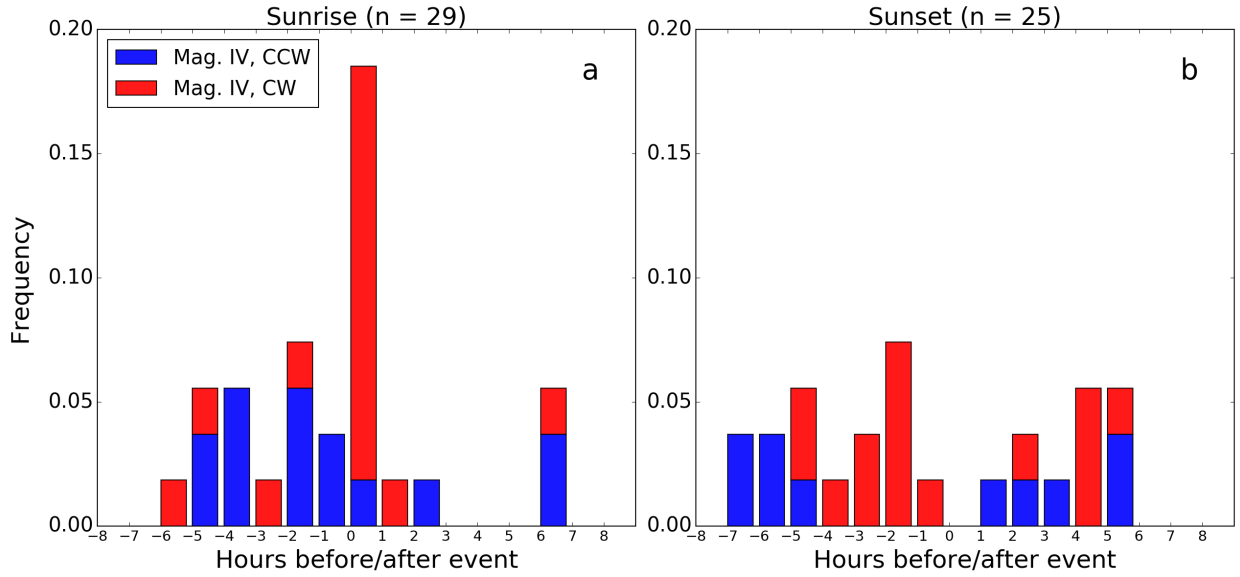

Figure 3.6: Magnitude IV rotations (as in Figure 3.5) color coded by rotational direction: counterclockwise (blue) or clockwise (red).

Wind speed during rotations

Wind speeds around the morning and evening transitions are typically low because the horizontal pressure gradient that develops during the night or day is in the process of weakening and reversing (Whiteman 2000). Because Magnitude IV rotations are expected to happen mainly during these transitional periods, it follows that wind speeds during these rotations should be relatively low. On the other hand, Magnitude I rotations are observed consistently throughout the day and night, when upvalley and downvalley flows are well-established. Wind speeds during these small rotations should be relatively high.

Figure 3.7 shows histograms of wind speed observations during wind rotations. The distributions are visually similar, with some slight differences between the rotational categories. Magnitude I and II rotations have distributions of similar shape, with a slightly wider peak

and a slightly thicker tail in the Magnitude I distribution. Wind speeds during Magnitude IV rotations have a shape similar to that in the Magnitude I distribution, but shifted left (toward lower wind speeds). To compare these distributions, a Kolmogorov-Smirnov test was applied pairwise (six tests in total). The six tests returned a p-value of $p < 0.001$, indicating that all distributions are significantly different from one another. This implies that wind speeds are typically lower during large rotations and higher during small rotations. Boxplots of the distributions show similar medians and interquartile ranges for the four categories, but with many more high wind speed outliers during Magnitude I and II rotations (Figure 3.8).

Rotation sensitivity analysis

The divisions for the four rotational magnitude categories were chosen for physical reasons relating to the thermally-driven orographic wind system. However, the minimum time threshold of 10 minutes to define a rotation was chosen somewhat arbitrarily. To test the sensitivity of rotation identification algorithm to this time threshold, the filtered climatology was passed through the algorithm with various thresholds ranging from 5 to 20 minutes (Table 3.2). Magnitude I rotations are the most sensitive to changes in the time threshold, with 1023 rotations identified with a 5-minute threshold and only nine rotations identified with a 20-minute threshold. On the other end of the spectrum, the total number of Magnitude IV rotations changed from 64 at a 5-minute threshold to 26 at a 20-minute threshold. However, because of the large decrease in Magnitude I rotations as the time threshold increased, Magnitude IV rotations represented only 4% of all rotations with a 5-minute threshold, but increased to 42% of all rotations with a 20-minute threshold. The 10-minute threshold chosen for the primary analysis is a good middle ground that includes a reasonable number of Magnitude IV rotations, while not over-representing Magnitude I rotations.

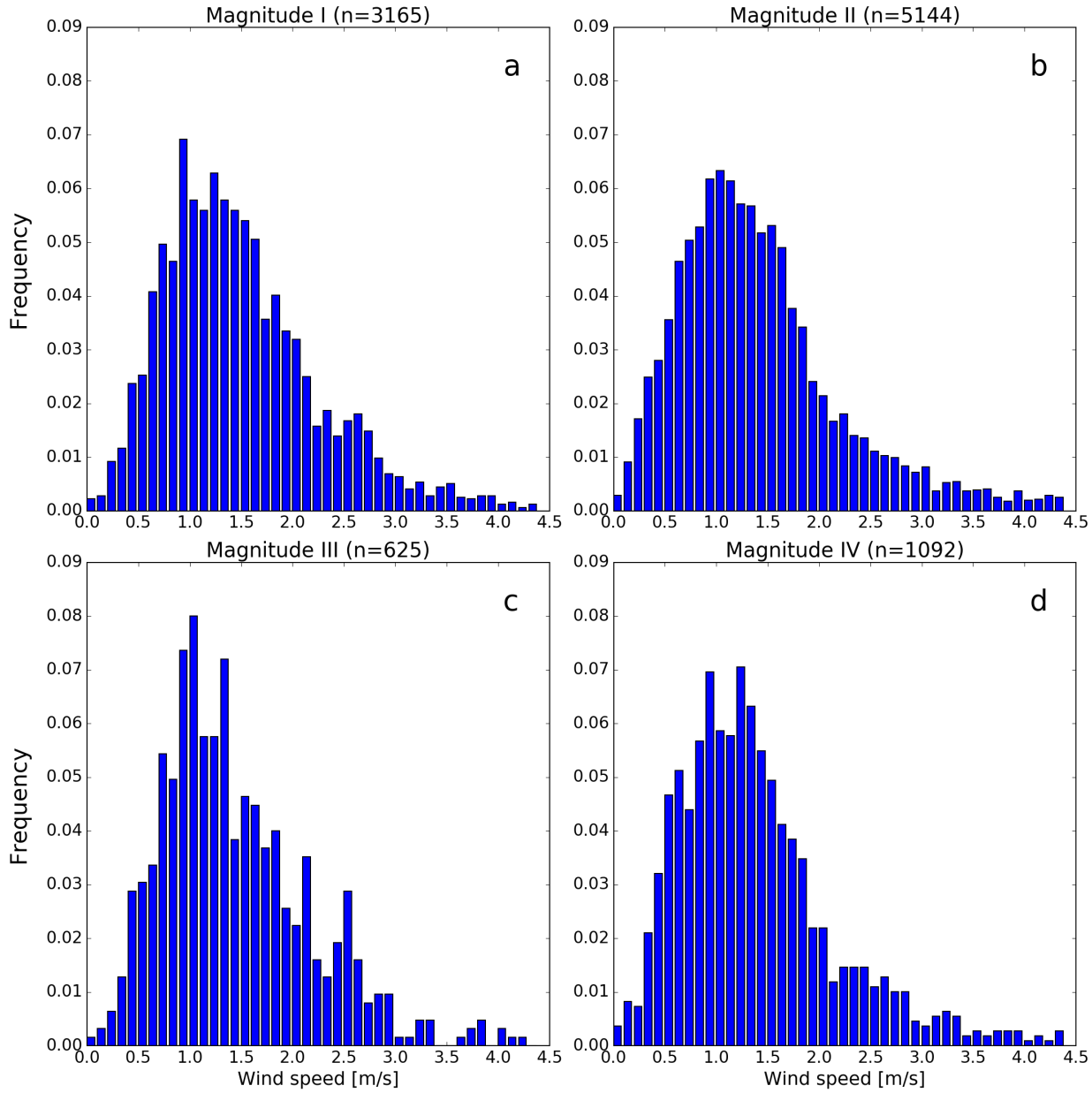

Figure 3.7: Distributions of wind speed during a) Magnitude I, b) Magnitude II, c) Magnitude III, and d) Magnitude IV rotations. The bin width for all histograms is 0.1 m s^{-1}.

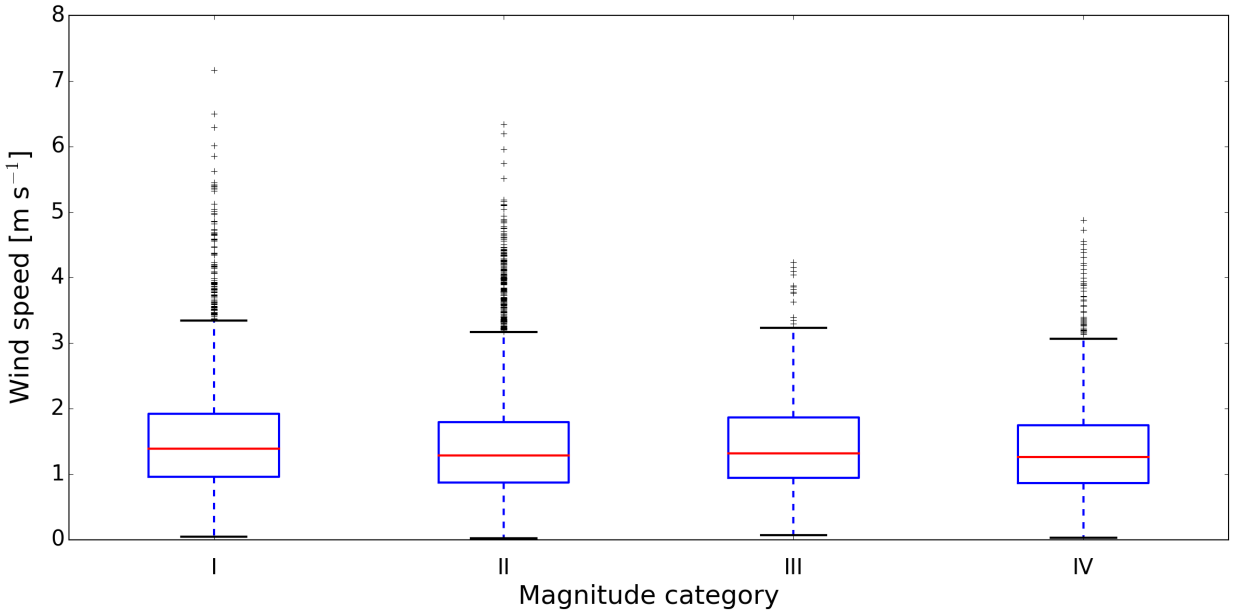

Figure 3.8: Boxplots of wind speed during rotations. Median wind speeds marked by red lines. First and third quartiles marked by boundaries of blue boxes. Whiskers (dashed blue line) extend from first and third quartiles a distance of 1.5 times the interquartile range. Wind speed observations outside whiskers are marked with a +.

Table 3.2: Rotations identified with various minimum time threshold. Threshold value is given in minutes. For each magnitude category, the number of rotations is given, followed by the percentage of total rotations represented by that category.

Thresh	Total	Mag I	Mag II	Mag III	Mag IV
5	1717	1023 (59%)	576 (34%)	54 (3%)	64 (4%)
8	1056	447 (43%)	501 (47%)	46 (4%)	62 (6%)
10	800	278 (35%)	426 (53%)	42 (5%)	54 (7%)
15	178	34 (19%)	82 (46%)	18 (10%)	44 (25%)
18	102	17 (17%)	44 (43%)	9 (9%)	32 (31%)
20	63	9 (14%)	21 (33%)	7 (11%)	26 (42%)

3.4.2 Northeasterly winds

Distributions of wind speed and direction for the filtered climatology and for the eclipse day can be summarized with wind roses (Figure 3.9). The two wind roses have similar shapes, with a somewhat-bimodal distribution between northwesterly (downvalley) and southeasterly (upvalley) winds. Northeasterly winds make up only a small percentage of both plots, representing 4.7% of climatological observations and 8.5% of eclipse observations.

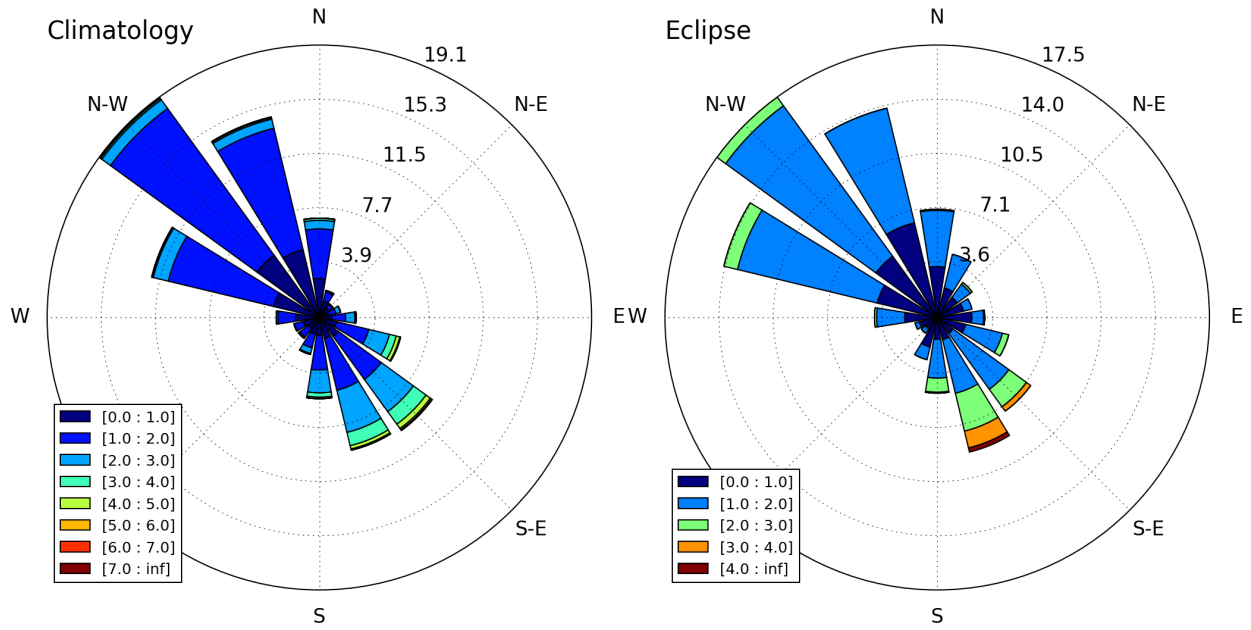

Figure 3.9: Wind roses of the filtered climatology (left) and eclipse day (right). Colored shading by wind speed (m s^{-1}). Numbers in the compass plot represent frequencies of wind direction.

While the wind roses are useful for summarizing the observations from both periods, they do not convey any information about the timing of winds. Figure 3.10 shows the distribution of northeasterly winds in the wind roses relative to the nearest sun event (similar to Figure 3.4). Nearly 18% of all northeasterly wind in the filtered climatology occurs 1-2 hours after sunrise. This particular hour experiences northeasterly wind more than two times more frequently than any other hour relative to either sunrise or sunset. This result is compatible, and perhaps expected, alongside the rotational results from Figure 3.6 and the conceptual diagram presented in Chapter 2 (Figure 2.10). During the morning transition, winds typically

rotate CW from downvalley to upvalley. As upslope winds form over the western sidewall, northeasterly winds from the small hill begin to penetrate further into the convergence zone. Additional observations with a dense network of surface weather stations would help determine more detailed mechanics of wind patterns during the morning transition.

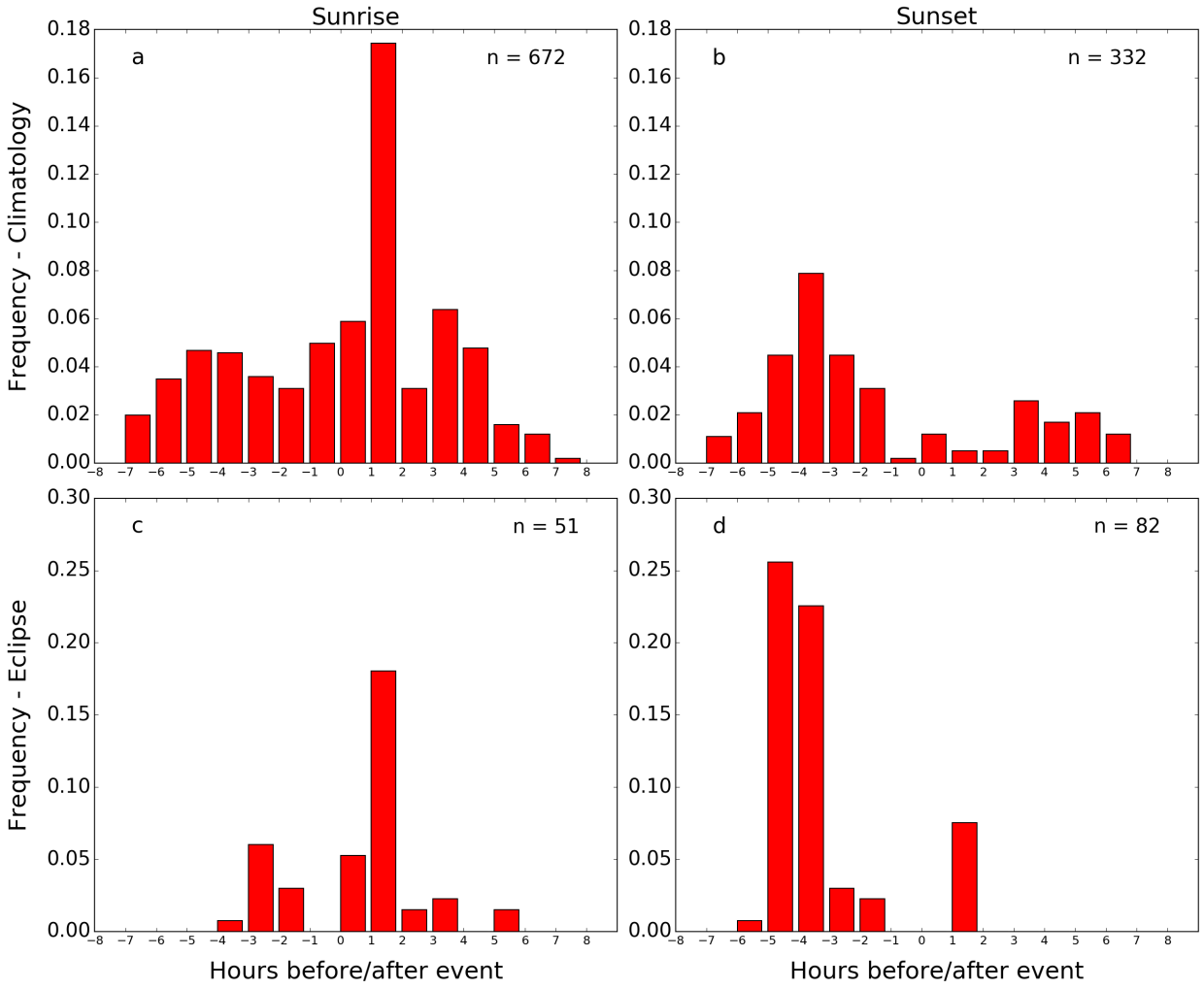

Figure 3.10: Distribution of northeasterly winds in filtered climatology (top row) and eclipse data (bottom row) relative to sunrise and sunset (as in Figure 3.4). The subplots in each row are normalized using the number of observations in the respective row (i.e. $n = 1004$ for the climatology and $n = 133$ for the eclipse.) Note the different limits in the y-axes between the two rows.

Wind observations from the eclipse day also show a relatively large percentage of northeasterly wind 1-2 hours after sunrise, indicating that conditions around sunrise were thermally-driven. However, northeasterly wind 3-5 hours before sunset on eclipse day deviates sub-

stantially from the climatology. This sharp contrast provides additional evidence that the northeasterly wind on 21 August was a direct result of the eclipse, and not due to other factors. Fisher's Exact test was used to determine if the distributions in Figure 3.10 are significantly different. Fisher's Exact test is preferable to the χ^2 test for contingency tables when the number of expected observations in a given category is less than 5 (Sheskin 1997), which is the case for the distributions in Figure 3.10. Fisher's Exact test returns a p-value of $p < 0.001$, indicating the distribution of northeasterly wind on the eclipse day is significantly different from the climatological distribution.

3.4.3 Synoptic conditions

Results from this climatological analysis show that certain terrain-wind interactions happen regularly at Innisfree. However, any recognizable patterns have been identified with surface observations only. Future studies to collect observations of the lower ABL on thermally-driven days, employing the tethered balloon and Doppler lidar, could significantly enhance understanding of these patterns and interactions. The synoptic weather conditions on the dates in the filtered climatology can be examined to improve the success of such studies. Since the conditions on these dates allowed for thermally-driven flows to develop at Innisfree, planning future field campaigns around similar weather conditions will improve the chances of observing the vertical structure of thermally-driven flows.

Figures 3.11 and 3.12 show NARR daily composites of 850 mb geopotential heights and winds, respectively, for each day in the filtered climatology. Figures 3.13 and 3.14 show NARR composites of 850 mb geopotential heights and winds for the entire filtered climatology (i.e. the average of all heights and winds in Figures 3.11 and 3.12). The composite geopotential for the filtered climatology, and many of the daily composites, show Virginia under the influence of a high pressure system. In Figure 3.13, a relatively weak pressure gradient is present over Virginia, with 850 mb heights dropping less than 5 m over the entire

state from south to north. With this weak synoptic pressure gradient, local orographic pressure gradients are able to form without interruption from larger-scale patterns. The weak synoptic pressure gradient also results in low wind speeds at 850 mb (Figure 3.14). Winds over Virginia barely reach 3 m s^{-1} near the Eastern Shore, and are closer to 2 m s^{-1} near Innisfree. These low synoptic wind speeds are unlikely to disrupt expected diurnal patterns of thermally-driven winds. Future studies at Innisfree that focus on the morning and evening transitions or the vertical structure of thermally-driven flows should take these conditions into account, and plan measurements around similarly forecasted conditions.

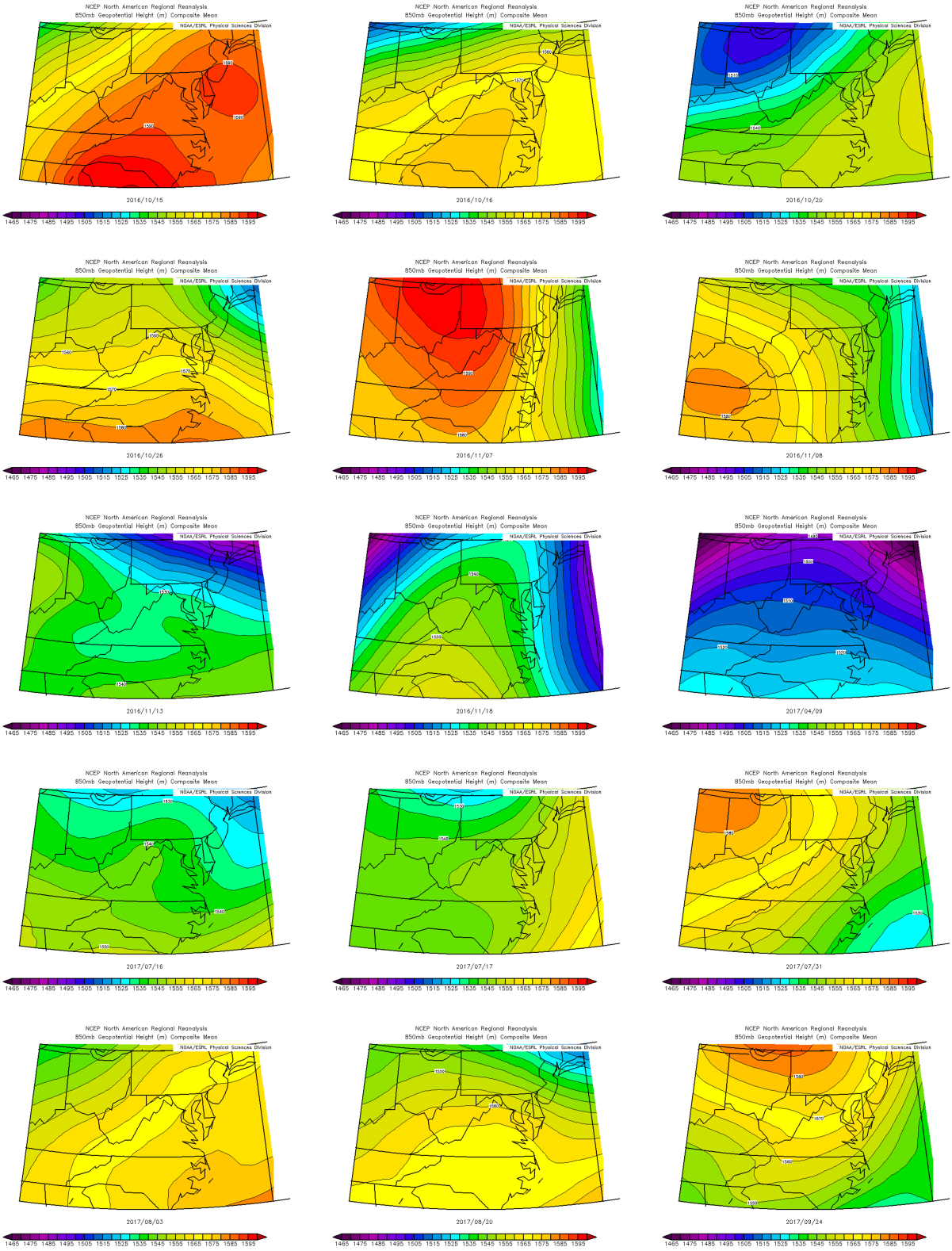

Figure 3.11: 850 mb geopotential heights for each day in the filtered climatology. The colorbar scale of 1465-1600 m is uniform across all subplots. NARR data provided by the NOAA/OAR/ESRL PSD, Boulder, Colorado, USA.

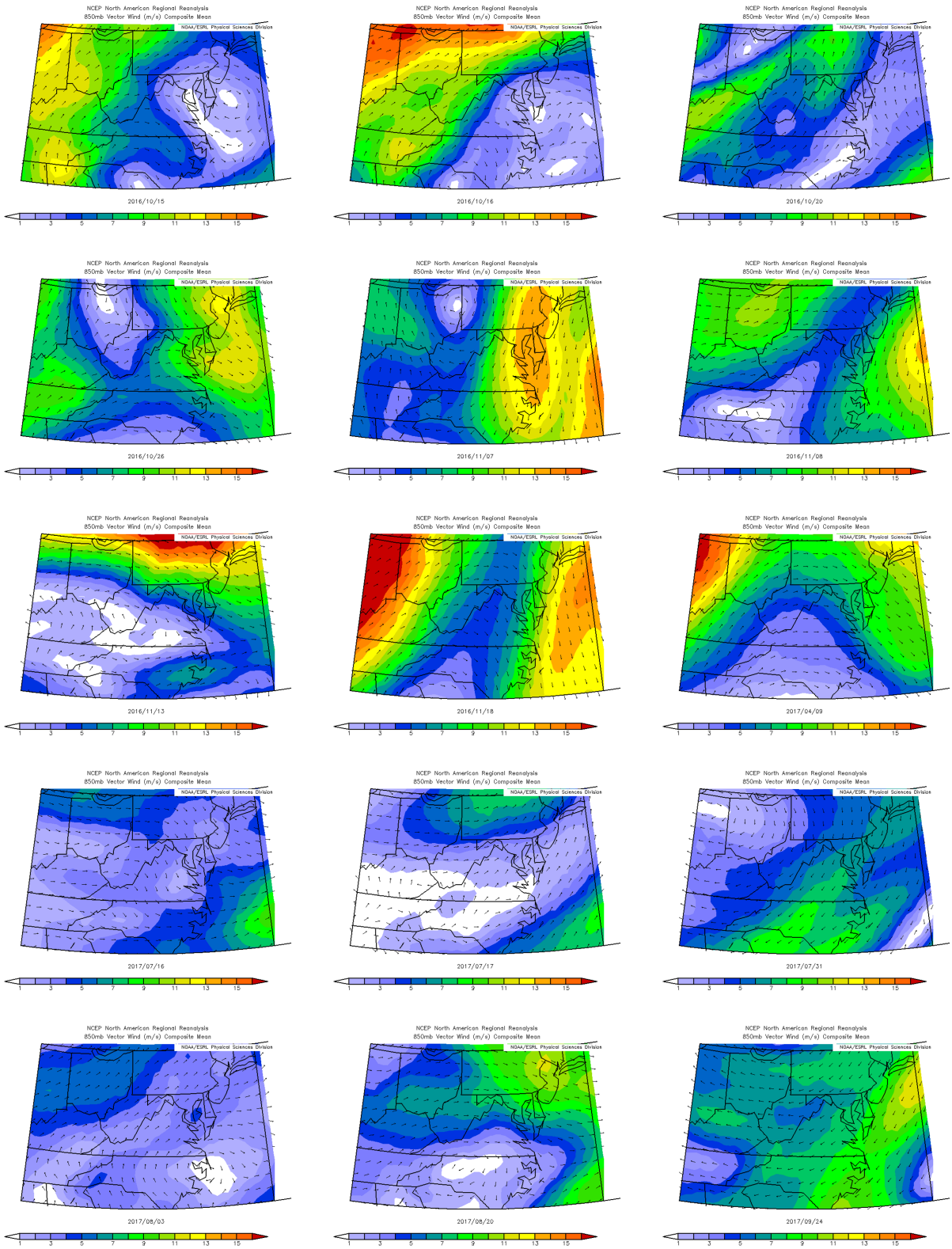

Figure 3.12: 850 mb wind speed (shading, m s^{-1}) and wind direction (vectors) for each day in the filtered climatology. The colorbar scale of 1-16 m s^{-1} is uniform across all subplots. NARR data provided by the NOAA/OAR/ESRL PSD, Boulder, Colorado, USA.

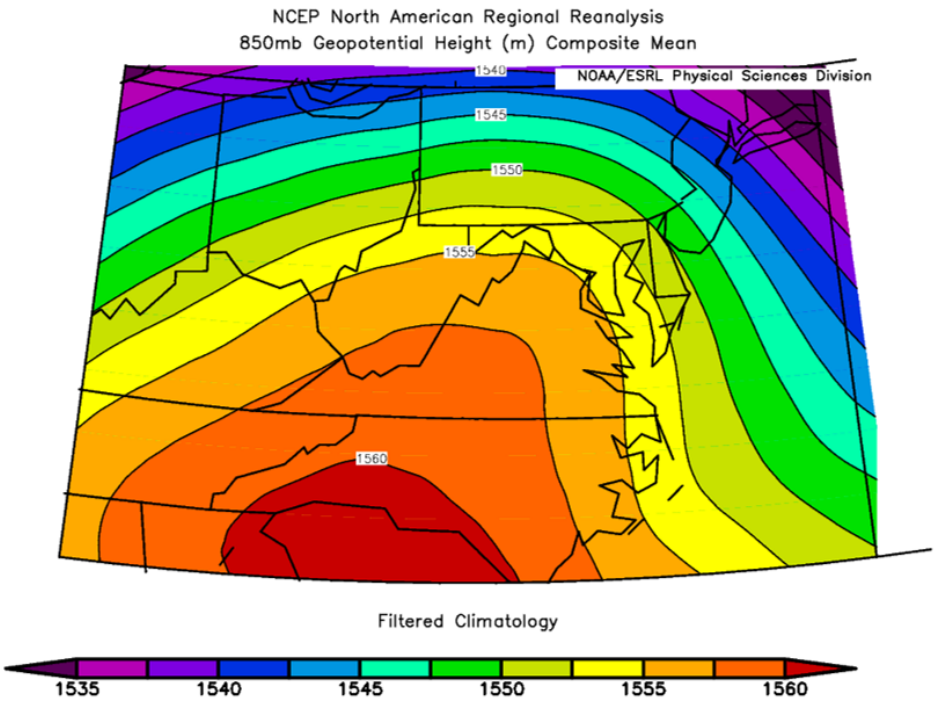

Figure 3.13: 850 mb composite geopotential height for the filtered climatology. NARR data provided by the NOAA/OAR/ESRL PSD, Boulder, Colorado, USA.

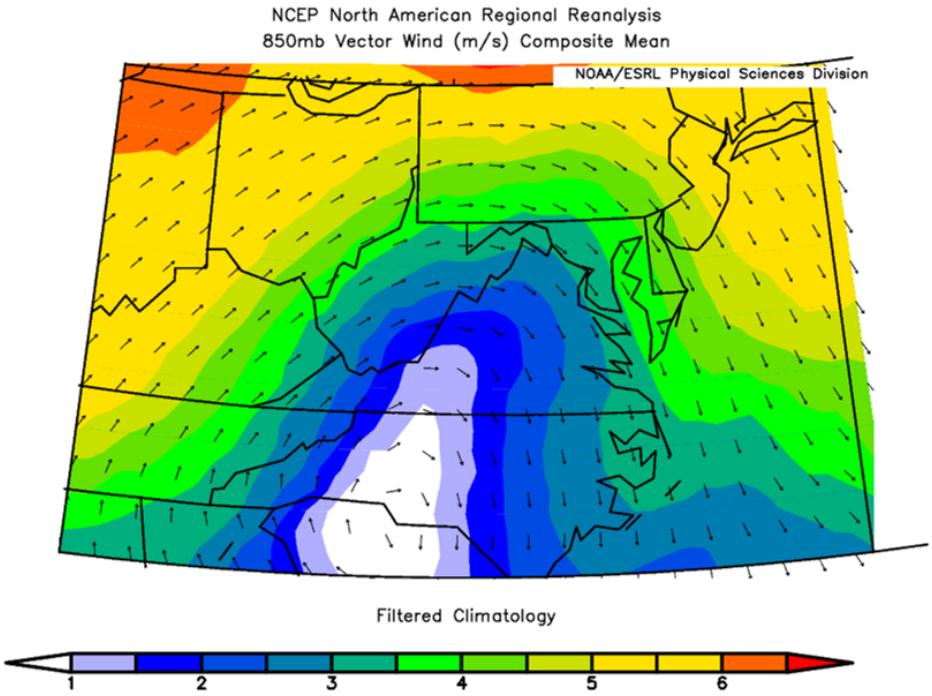

Figure 3.14: 850 mb composite wind speed (shading, m s^{-1}) and wind direction (vectors) for the filtered climatology. NARR data provided by the NOAA/OAR/ESRL PSD, Boulder, Colorado, USA.

3.5 Summary and Conclusions

This chapter focused on a climatological analysis of wind observations at Innisfree. The main research objectives were to define 'typical' conditions during thermally-driven morning and evening transition periods, and compare observations taken during these periods to observations from the eclipse event on 21 August 2017. After a year-long dataset was passed through three rounds of filtering, a total of 15 days were representative of true thermally-driven conditions. Wind rotations and periods of northeasterly winds were identified in this filtered climatology for comparison to the eclipse day. The main results are as follows:

- Magnitude IV rotations most frequently occur 1-2 hours after sunrise in the clockwise direction. This result provides support for the conceptual diagram of terrain-wind interactions presented in Chapter 2. Northeasterly winds from the small hill continue during the morning transition, which causes the rotation from downvalley to upvalley to occur in the clockwise direction.

- Northeasterly winds made up only a small percentage of wind observations from both the filtered climatology (4.7%) and the eclipse day (8.5%). However, the distributions of northeasterly winds with respect to sunrise and sunset were significantly different between the two datasets. In the climatology, northeasterly winds occur most frequently 1-2 hours after sunrise, aligning closely with the morning transition wind rotation. The day of the eclipse featured northeasterly winds not only during the morning transition, but also during the late afternoon hours.

- Magnitude IV rotations (>135 degrees) make up only 7% of all rotations at Innisfree when a 10 minute time threshold is used to identify rotations. Changing this time threshold has a significant effect on the number of flagged Magnitude I rotations (<30 degrees), but does not result in a drastic change in the number of Magnitude IV rotations.

- Composites of 850 mb geopotential height from the filtered climatology indicate that thermally-driven conditions are likely to develop at Innisfree when Virginia is under the influence of a high pressure system.

This climatological analysis indicates that the wind rotations and northeasterly wind during the eclipse event are not remarkable on their own. Instead, what makes the eclipse observations stand out is the time of day when the rotations and northeasterly wind occurred. Additionally, the winds that developed on the afternoon of the eclipse shared some characteristics with morning and evening transition winds, but ultimately took a form distinct from either transitional period. It is clear that conditions on the morning of the eclipse were thermally-driven, and that wind patterns on that afternoon are directly attributable to the eclipse.

The method of filtering the year-long climatology to identify thermally-driven days is not limited to this particular valley. This method could be employed during site selection for a future air pollution point source (e.g. a manufacturing facility or power plant) in any valley. The additional analysis of wind rotations on thermally-driven days could give an indication of the extent to which such rotations may affect air quality and aerosol dispersion in a given valley.

The climatological analysis has also identified synoptic weather patterns that may favor the development of thermally-driven winds at Innisfree. Future field campaigns at Innisfree can be planned around similar synoptic conditions. A dense network of surface weather stations installed on and near the small hill could provide additional insight into the mechanics behind northeasterly winds during morning transitions. Future work at Innisfree should also involve vertical observations of the ABL during the morning and evening transitions on thermally-driven days. The present study has shown that certain wind patterns tend to form at the surface during transition periods, but observations of the vertical structure of the ABL during these times do not exist at this climatological level. Detailed vertical observations

during thermally-driven transitions would provide additional information about the extent to which wind rotations propagate above the valley floor, another important consideration for air quality within valley atmospheres.

Chapter 4

Summary and conclusions

The primary goal of this thesis project was to observe thermally-driven winds in Innisfree valley during the 21 August 2017 solar eclipse, and to interpret those observations in the context of climatological morning and evening transitions at study site. Important results from the analysis of the eclipse and climatological analysis include:

- Surface cooling during the eclipse at Innisfree was more than two standard deviations larger than the average of all solar eclipse events compiled by Eugster et al. (2017). This cooling caused the formation of a stable layer at the surface.

- Surface weather stations recorded multiple rotations in wind direction during and after the eclipse. Slope and valley flows both contributed to these rotations. The size and direction of the rotations were strongly influenced by the proximity of the stations to local terrain features.

- Tethered balloon and lidar observations showed that wind shifts and rotations were not limited to the surface. A layer of downvalley winds formed between the surface and ∼300 m AGL during the second half of the eclipse. Winds above this layer remained upvalley or westerly. The timing of this wind layering indicates a time lag between decreased radiation during the eclipse and the reversal of the horizontal temperature

gradient. Downvalley wind was not initiated until ∼80 minutes after the start of the eclipse, and appeared in the ABL after convection was re-initiated at the surface. The downvalley wind layer existed for ∼70 minutes and dissipated shortly after final contact.

- In the climatological record, Magnitude IV rotations most frequently occur 1-2 hours after sunrise in the clockwise direction. Northeasterly winds near the small hill continue during the morning transition, which causes the rotation from downvalley to upvalley to occur in the clockwise direction.

- Northeasterly winds made up only a small percentage of wind observations from both the filtered climatology (4.7%) and the eclipse day (8.5%). However, the distributions of northeasterly winds with respect to sunrise and sunset were significantly different between the two datasets. In the climatology, northeasterly winds occur most frequently 1-2 hours after sunrise, aligning closely with the morning transition wind rotation. The day of the eclipse featured northeasterly winds not only during the morning transition, but also during the late afternoon hours.

- In the climatological record, Magnitude IV rotations (>135 degrees) make up only 7% of all wind rotations at Innisfree. Changing the minimum time threshold to define a rotation has a significant effect on the number of flagged Magnitude I rotations (<30 degrees), but does not result in a large change in the number of Magnitude IV rotations.

- Composites of 850 mb geopotential height from the filtered climatology indicate that thermally-driven conditions are likely to develop at Innisfree when Virginia is under the influence of a high pressure system.

The main conclusions of the project are as follows:

- The decreased radiation and associated cooling during the solar eclipse altered the normal cycle of thermally-driven winds at Innisfree. In regard to incoming solar radi-

ation, the first and second halves of the eclipse are similar to the evening and morning transitions, respectively, but with important differences caused by the orientation of the topographic features relative to the solar elevation and azimuth angles. The high elevation and low azimuth angles during the eclipse caused different wind patterns to develop than what would typically be expected during the transition periods.

- The wind patterns that developed during the eclipse are remarkable because of the time of day when the rotations and northeasterly wind occurred. These winds shared some characteristics with typical morning and evening transition winds, but ultimately took a form distinct from either transitional period. It is clear that conditions on the morning of the eclipse were thermally-driven, and that wind patterns on that afternoon are directly attributable to the eclipse.

- Wind observations taken during the eclipse the eclipse indicate that rotating winds, previously described over valley sidewalls, can also be present at locations on or above the valley floor. The magnitude and direction of rotation at various locations over the valley floor appears to vary between the morning and evening transitions, and is also dependent on local terrain features.

Future studies at Innisfree should be planned with a focus on observing wind rotations in the lower atmosphere during thermally-driven morning and evening transition periods. After the present study, it is apparent that these rotations exist at the surface of valley floor sites. A better understanding of the timing, structure, and magnitude of such rotations above the surface is important for air pollutant dispersion and air quality within a valley.

Appendix A

Full instrumentation list

Additional instrumentation was installed at the investigation area for the eclipse experiment that was not used for analysis in Chapter 2. The purpose of this appendix is to provide a list of all additional operational instruments during the eclipse, and to provide a brief description of the observations made by those instruments. Instrumentation already described in Chapter 2 is not repeated here. A site map that includes all instruments (even those described in Chapter 2) is shown in Figure A.1.

A.1 HOBO T/RH grid

Sixteen HOBO Pro v2 temperature and relative humidity sensors were deployed in a 4×4 grid to measure the spatial variability of the two variables over a relatively flat section of the valley floor. Each of the sensors was installed inside a naturally ventilated Onset RS3 radiation shield. Similar to the Onset thermohygrometers installed on the main tower, the HOBO temperature and humidity sensors have response times of approximately 5 minutes. Even with this relatively slow response time, the gridded array of sensors is able to provide some information about the spatial variability of temperature and humidity during the eclipse.

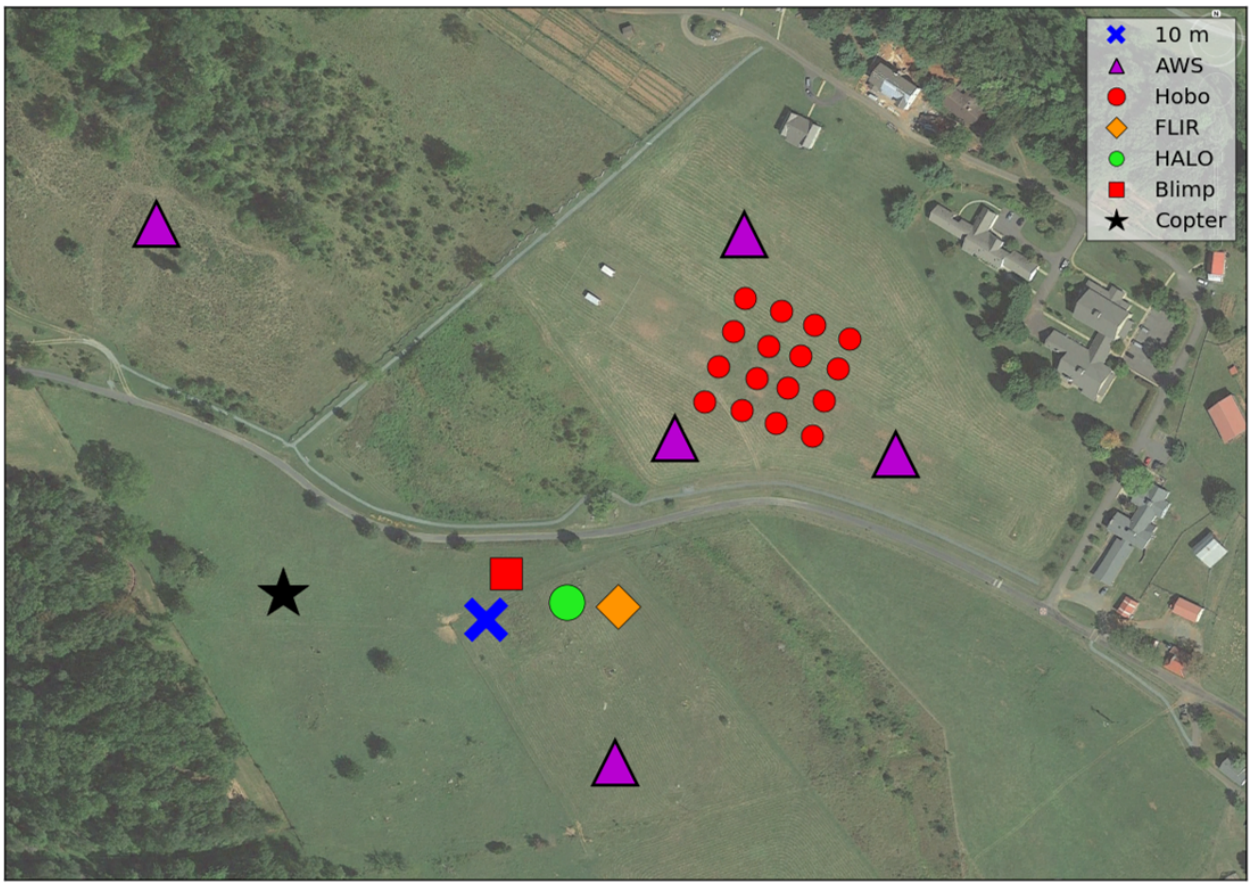

Figure A.1: Map showing layout of all instrumentation installed during the solar eclipse field campaign.

A.2 FLIR cameras

The spatial variability of surface temperature during the eclipse was captured with a FLIR T450sc infrared camera. The camera was mounted in a tripod near the main tower and pointed toward the northeast. In the field of view of the FLIR camera was a flat section of the valley floor where three AWS and the HOBO grid were installed. The camera was programmed to capture an image every fifteen seconds between 12:00 and 18:00 EDT on 21 August. Two examples of the images collected on 21 August are shown in Figure A.2.

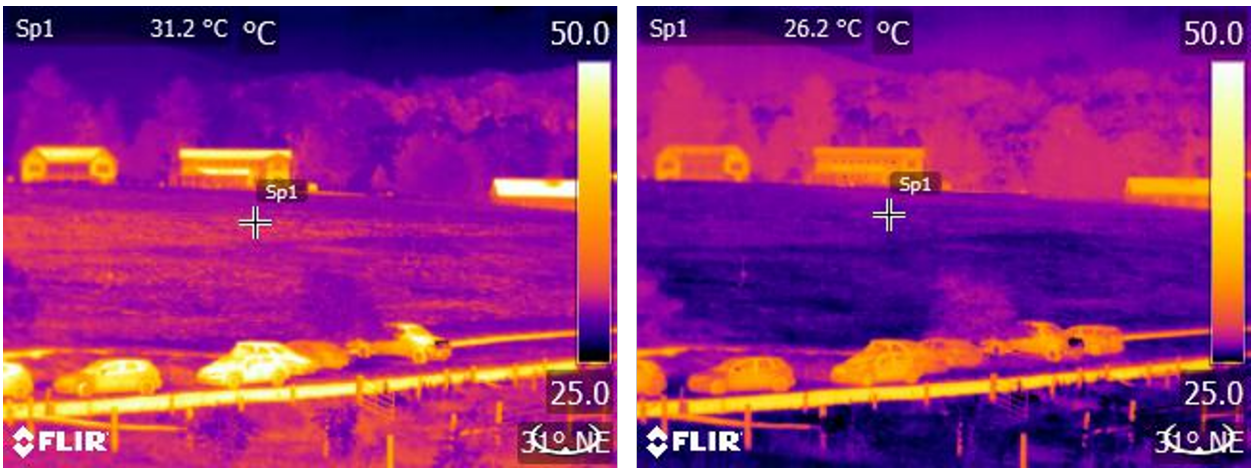

Figure A.2: Examples of the images taken with the FLIR camera during the eclipse. Left panel taken at first contact; right panel taken at maximum eclipse.

In addition to the ground-based infrared camera, a FLIR Tau 2 infrared camera was mounted to a DJI S900 hexacopter unmanned aerial vehicle (UAV). This FLIR-UAV system was deployed several times during the eclipse to take overhead aerial photos of the same field which was captured by the FLIR T450sc. The resulting photos provide surface temperature measurements of the field from a second angle.

A.3 UAV-based vertical profiles

As a complement to the tethered balloon system, a multirotor UAV was utilized to gather vertical profiles of temperature and humidity using an iMet XQ sensor (http://www.intermetsystems.com/prod xq). In addition, a Sparv Embedded Windsond sensor attached to the bottom of the UAV collected temperature and humidity measurements while the UAV ascended at a rate of 1 m s^{-1}. The mechanism that attached the Windsond to the UAV was a clamp that could be remotely operated. At a height of approximately 100 m AGL the clamp was opened, releasing the Windsond sensor, which was attached to a small plastic parachute. This dropsonde system allowed for descending profiles of temperature and humidity that sampled undisturbed air.

A.4 Morning tethered balloon profiles

Tethered balloon profiles were collected on the morning of 21 August using the same technique described in Section 2.3.4. These profiles are included here in Figure A.3. The profiles show a surface-based temperature inversion in the early morning hours coinciding with northerly flows throughout the column. Shortly after sunrise at 7:01 EDT, winds were calm (< 0.5 m s^{-1} throughout much of the column. During the morning transition, winds move between southwesterly and easterly before southeasterly upvalley flow is finally established in profile 13. By this time temperatures throughout the column were approaching 26 C. These morning profiles provide additional evidence that easterly winds during the morning transition extended throughout a layer of the ABL, and were not confined to the surface.

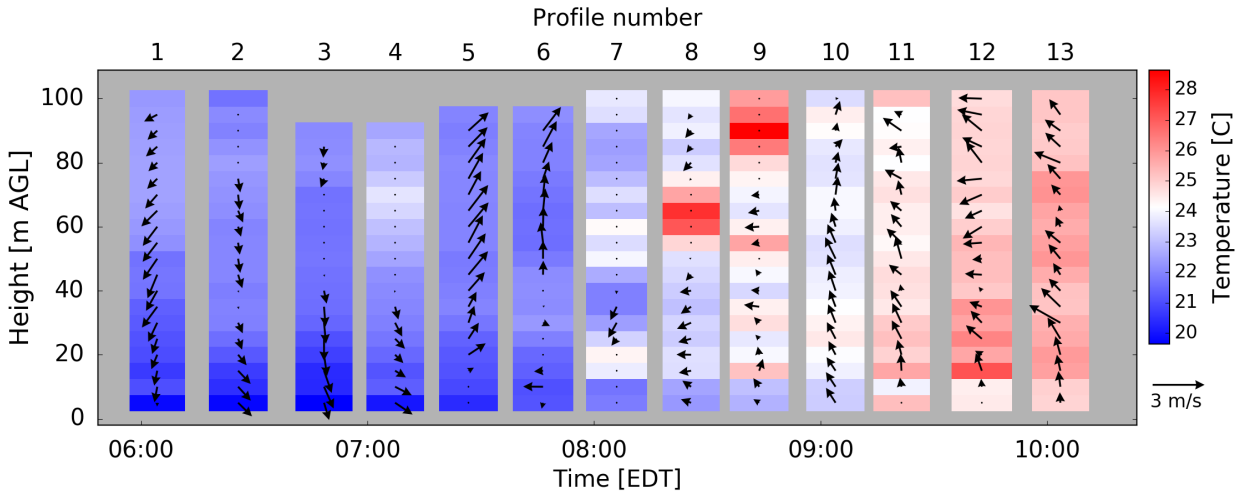

Figure A.3: Vertical profiles of temperature (shading) and horizontal winds (vectors) collected by the tethered balloon on the morning of 21 August. The first profile begins at 05:57 EDT and the final profile begins at 09:56. Ascent rate of the balloon was 10 m every 90 s. Temperature and wind data collected by the Kestrel 4500 were bin-averaged every 5 m for this figure. The orientation of the wind vectors is such that a vector pointing to the top of the page indicates a southerly wind.

Appendix B

Instrument comparison

This appendix presents a comparison of observations made by similar instruments installed on the main tower during 21 August 2017. Temperature observations made by aspirated and non-aspirated temperature sensors are compared, as are observations of wind speed and direction made by the sonic and propeller anemometers.

B.1 Aspirated vs. non-aspirated temperature sensors

Temperature measurements on 21 August 2017 were made by two separate instrumentation systems. The first system consisted of two Onset S-THB-M002 thermohygrometers in non-aspirated radiation shields, installed at 2.0 m and 9.4 m AGL. This system was installed on the main tower in August 2016 and provided the climatological temperature measurements used for analysis in Chapter 3. The second system consisted of two Apogee ST-110 thermistors housed in aspirated radiation shields, also installed at 2.0 m and 9.4 m AGL. These thermistors were installed in May 2017 specifically for the solar eclipse field campaign. The thermistors have a much faster response time than the thermohygrometers (5 seconds as opposed to 5 minutes) which made them ideal for capturing the rapid response of the atmo-

spheric boundary layer to the solar eclipse. The aspirated radiation shield constantly draws air over the thermistors, which further reduces artificially-high temperature measurements caused by radiation error.

On 21 August the non-aspirated sensors sampled at 1 Hz, while the aspirated sensors sampled at 0.2 Hz. Despite the slower sampling rate, the aspirated sensors show temperature changes at a much finer time scale due to their faster response time (Figure B.1). At night, differences in 2 m temperature between the two sensors were relatively small, with the non-aspirated sensor recording temperatures $\sim$0.2 C warmer than the aspirated sensor. Shortly after sunrise the temperature difference began to rise, and throughout the morning and early afternoon hours the difference was 1-2 C. For a brief period around 10:00 EDT the temperature difference approached 3 C. During and after the eclipse, the temperature difference decreased, but temperatures recorded by the non-aspirated sensor were consistently warmer throughout the day than those recorded by the aspirated shield. The temperature difference fell below 0.5 C shortly after sunset, but exhibited a higher variability than the temperature difference in the early morning hours. This is because the stable boundary layer is still forming in the hours after sunset, while the boundary layer in the early morning hours is more stable.

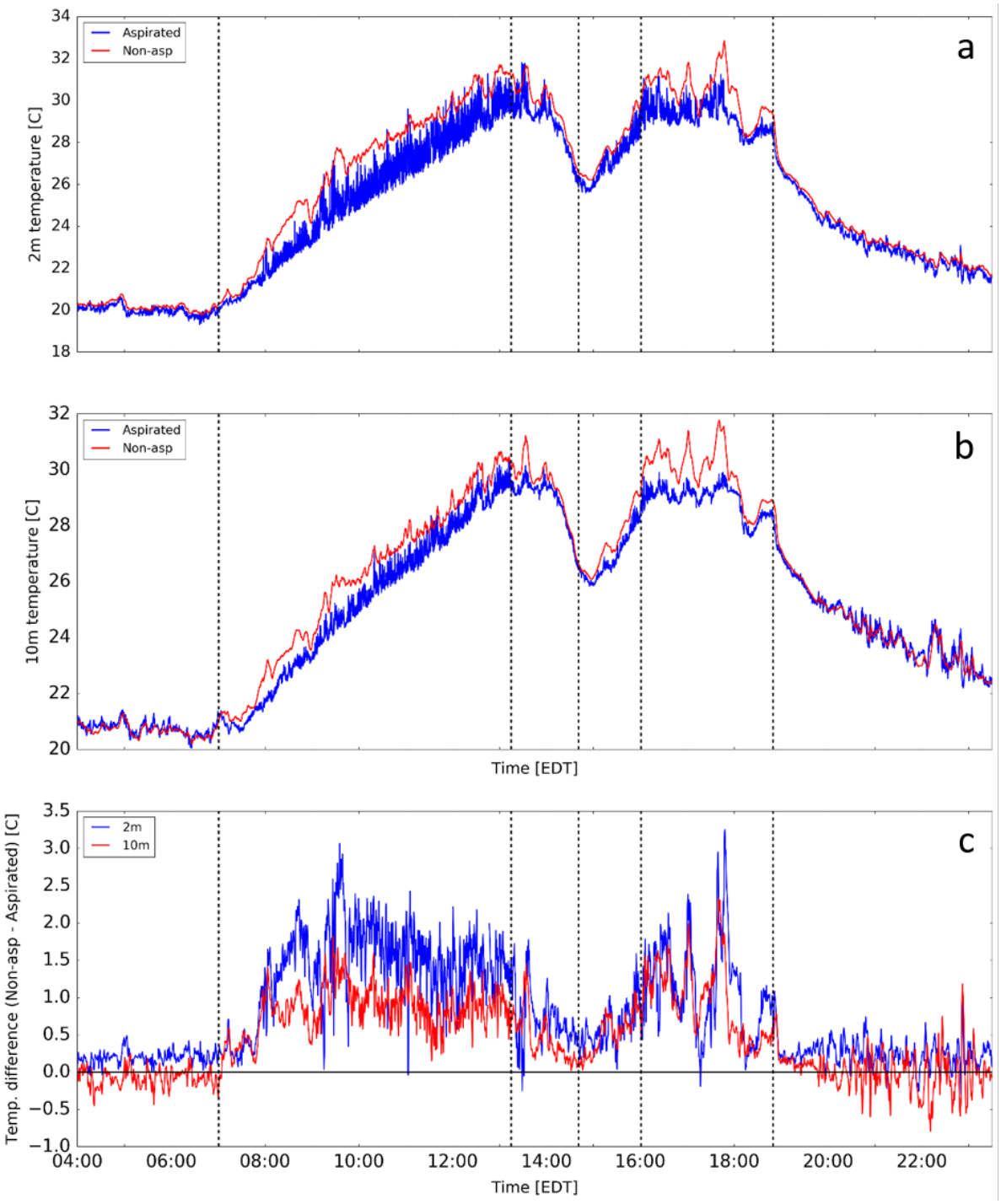

Figure B.1: a) A comparison of 2 m temperatures measured by the aspirated thermistor (blue line) and non-aspirated thermohygrometer (red line) on 21 August 2017. b) Similar to top panel, but with 10 m temperature. c) Temperature difference between non-aspirated and aspirated temperature sensors at 2 m (blue line) and 10 m (red line).

B.2 Sonic vs. propeller anemometer

Only observations from the sonic anemometer were presented in Chapter 2, but propeller anemometer data were used during the climatological filtering process described in Chapter 3. As described in that chapter, observations from the sonic anemometer should be more accurate, especially at low wind speeds (see Section 3.2.3 for additional discussion). A comparison of wind speeds measured on 21 August confirms that some winds captured by the sonic anemometer were too weak to spin the propeller (Figure B.2a, b). In these instances, the propeller anemometer recorded wind speeds of 0 m s^{-1}. This behavior is especially apparent in the early morning hours, and in the post-eclipse afternoon hours. A comparison of wind direction measured by the two anemometers shows relatively small differences of $\sim$5 degrees of less throughout the day (Figure B.2c, d). Larger differences in wind direction occur during periods of rotating winds, especially during the morning and evening transitions and the post-eclipse afternoon hours. During such rotations, the sonic anemometer registers the wind rotations more rapidly than the propeller anemometer, resulting in differences of 15 degrees or more.

To quantify differences in wind speed and direction, bias (Eq. B.1) and mean absolute error (MAE; Eq. B.2) were calculated during two periods representative of daytime and nighttime conditions. These periods were selected to avoid artificially inflating the bias or error values by including periods of wind rotations. The daytime period considered measurements between 9:00 and 16:00 EDT, and the nighttime period was between 19:00 and 21:00 EDT.

$$\frac{1}{n}\sum_{i=1}^{n}\left(D_i - \hat{D}_i\right) \tag{B.1}$$

$$\frac{1}{n}\sum_{i=1}^{n}|D_i - \hat{D}_i| \tag{B.2}$$

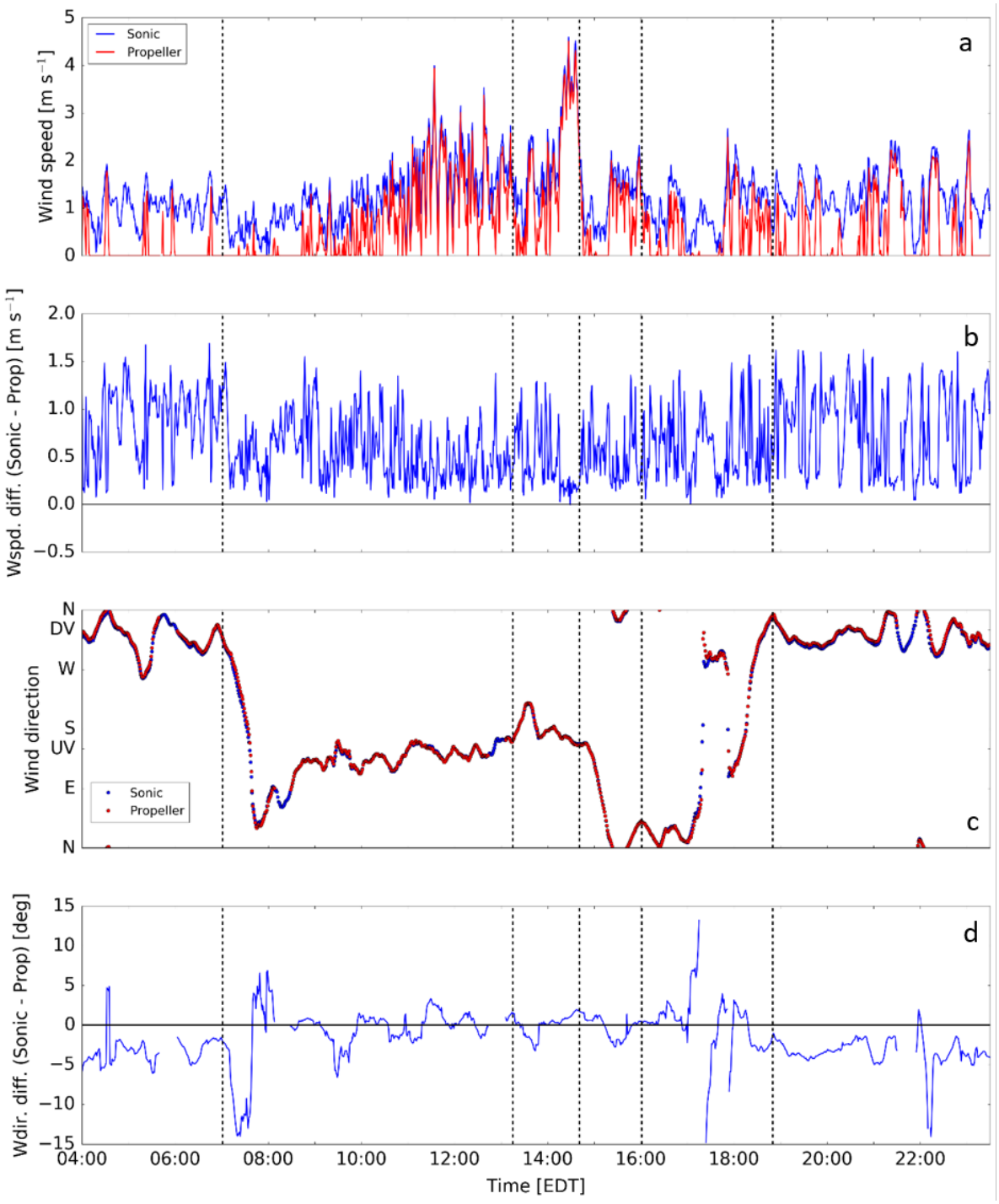

Figure B.2: a) Wind speed measured by the sonic (blue line) and propeller (red line) anemometers on 21 August. b) Difference between sonic and propeller anemometer wind speed. c) Wind direction measured by sonic (blue dots) and propeller (red dots) anemometers on 21 August. To reduce noise, a moving average with a 20-minute window was applied to the raw data. d) Difference between sonic and propeller anemometer wind direction.

Table B.1: Bias and mean absolute error (MAE) for wind speed and direction measurements from the propeller anemometer.

	Speed [m s^{-1}]		Direction [deg]	
	Day	Night	Day	Night
Bias	0.50	0.88	-0.3	1.2
MAE	0.50	0.88	-3.1	3.1

Bias and MAE values are shown in Table B.1. For wind speed, bias and MAE are the same because the propeller anemometer recorded a wind speed value faster than the sonic anemometer value for a given timestamp. The higher wind speed bias during the nighttime period is expected as calmer winds during these hours may be too weak to turn the propeller. Daytime wind direction values show almost zero bias, and MAE of just over 1 degree. This is well within the instrument tolerance. At night, sonic anemometer measurements were consistently from a more westerly direction than the propeller measurements, which is reflected by the fact that the wind direction bias and MAE are the same magnitude during the nighttime period. These calculations show that wind direction measurements between the two anemometers show good agreement during periods of relatively steady wind direction. Wind speed measurements can have some significant differences during transitionary and calm periods. Sonic anemometer observations should be used for accurate wind speed and direction data, especially during diurnal transitions and nighttime periods.

Appendix C

AWS calibration

The observations collected during the eclipse included two instances of the same measurements being made with multiple devices. For the tethered balloon profiles, two identical Kestrel 4500 Pocket Weather Tracker devices were used in alternating profiles. This setup allowed for a shorter break between profiles, as the data from one device could be downloaded as the other device was utilized for the next profile. Additionally, the five AWS deployed around Innisfree all consisted of the same set of instrumentation. In order to draw meaningful conclusions from the observations, it is important that the sensors on the separate devices are calibrated correctly. Correct instrument calibrations ensure that any differences or trends noted in the data are due to the physical processes in the valley, and not instrument error.

The Kestrel 4500 units were shipped to the manufacturer and received a factory recalibration on August 17, 2017. Since this service was performed so close to the eclipse event, no additional calibration testing was performed. The following sections describe the results of a calibration experiment for the anemometers on the five AWS deployed during the solar eclipse. Since wind direction was the main AWS variable considered in Chapter 2, it is also the focus of the following analysis.

C.1 Experimental design

The five AWS were removed from their installation locations during the eclipse and set up adjacent to the main tower. The configuration for this experiment was a line that began ∼5 m west of the main tower and continued toward the western sidewall. The AWS were placed approximately 5 m apart in an effort to sample the same air flow without one tower interfering with another tower's measurements. Measurement frequencies during this experiment were the same as during the eclipse (1 Hz for wind speed and direction). The AWS collected continuous measurements between 4-12 October 2017. A heavy rain event occurred on the night of 9 October into the morning of 10 October. Observations of wind direction from this period were not considered for the following analysis, in order to more accurately represent conditions similar to the eclipse day.

For each timestamp in the experimental period, the 'true' value for wind direction was taken to be the (circular) average of the measurements from each of the five AWS. Measurements from each AWS were compared to this average to assess the performance of each anemometer. Three metrics were used to summarize the performance of the AWS over the measurment period: bias (Eq. C.1), mean absolute error (MAE, Eq. C.2), and root mean square error (RMSE, Eq. C.3).

$$\frac{1}{n}\sum_{i=1}^{n}\left(D_i - \hat{D}_i\right) \tag{C.1}$$

$$\frac{1}{n}\sum_{i=1}^{n}|D_i - \hat{D}_i| \tag{C.2}$$

$$\sqrt{\frac{1}{n}\sum_{i=1}^{n}\left(D_i - \hat{D}_i\right)^2} \tag{C.3}$$

C.2 Results and discussion

Table C.1: Bias, mean absolute error (MAE), and root mean square error (RMSE) for wind direction observations from the five AWS during the experimental period (4-12 October 2017). Columns 2-4 show bias and error values for the raw data, while columns 5-7 show values for the bias corrected data. Bias was removed from AWS observations on an individual basis. All values given in degrees.

	No correction			Bias correction		
AWS	Bias	MAE	RMSE	Bias	MAE	RMSE
1	-10.60	13.55	20.3	-0.16	9.72	17.2
2	-10.89	12.85	16.7	-0.10	7.15	12.6
3	-8.82	13.43	19.7	-0.17	10.30	17.6
5	-0.94	20.19	31.7	-0.07	20.30	31.7
6	29.41	29.90	31.2	0.09	5.61	10.2

Table C.1 shows the bias, MAE, and RMSE for each of the five AWS over the experimental period. According to the manufacturer, the anemometers used on the AWS are accurate to ± 3 degrees. MAE values for all AWS are larger than this accuracy value, suggesting that the differences are not simply a result of instrument tolerance. Additionally, all AWS have RMSE values larger than MAE, which suggests that large outliers appear frequently in the observations across all stations. AWS6 has the largest bias by a factor of nearly 3. One possible cause for this bias could be an error during installation that resulted in the anemometer not pointing directly north. After removing the calculated bias from the observations, the MAE and RMSE for AWS6 become the lowest of the five stations. This provides additional evidence that the station was installed off of north for this period (in this case, it was pointing approximately 30 degrees east of north). AWS5 has an RMSE value similar to that of AWS6, but has a bias of less than one degree. Removing the bias from AWS5 observations does not affect the RMSE value, and actually increases the MAE slightly. This suggests that any large outliers in AWS5 observations are not necessarily due to a misalignment, but may be due to a non-calibrated or malfunctioning instrument.

Table C.1 shows that bias removal can improve the accuracy of AWS wind direction observations. All stations except AWS5 show improved MAE and RMSE values after bias removal.

Unfortunately the bias correction performed in Table C.1 cannot be applied in the same way to the solar eclipse data. The alignment of each AWS relative to north was almost certainly different during the two experimental periods. Additionally, the AWS during the solar eclipse were installed far apart and were sampling different wind fields in the valley. Hence, the technique of using the AWS average as the 'true' value would not be applicable for the solar eclipse observations.

Given the possibility of similarly high biases for the AWS during the solar eclipse, it is perhaps not appropriate to make any statements on absolute wind direction differences between any AWS, unless they vary by a significant amount (more than 30-40 degrees). The analysis of the eclipse results in Chapter 2 does not include comparison of these small differences in wind direction. Instead, the focus was on differences in downslope winds (northeasterly versus northwesterly - 60 degrees or more apart) and on rotational direction (clockwise versus counterclockwise). It is reasonable to assume that the anemometers on the AWS can accurately observe a large wind rotation (Marnitude III and IV; see Chapter 3) even if the directions at any point during the rotation are not exact. For these reasons, the conclusions drawn in Chapter 2 are resaonable, but caution should be used in future analysis of this data with regard to wind direction differences between individual AWS.

The design of the AWS permits the station (and therefore the anemometer) to rotate from a particularly strong wind gust. This is a design flaw that could be improved in future deployments by adding some new screws to the base of each AWS. If this is not possible, future AWS deployment should be done with great care to align the anemometers to north. This alignment should be checked regularly, especially during periods of high winds.

References

Anderson, J., 1999: Meteorological changes during a solar eclipse. *Weather*, **54 (7)**, 207–215, doi:10.1002/j.1477-8696.1999.tb06465.x.

Angevine, W. M., H. K. Baltink, and F. C. Bosveld, 2001: Observations of the morning transition of the convective boundary layer. *Boundary-Layer Meteorology*, **101 (2)**, 209–227, doi:10.1023/A:1019264716195.

Aplin, K. L., C. J. Scott, and S. L. Gray, 2016: Atmospheric changes from solar eclipses. *Phil. Trans. R. Soc. A*, **374 (2077)**, 20150 217, doi:10.1098/rsta.2015.0217.

Awan, N. K., H. Truhetz, and A. Gobiet, 2011: Parameterization-Induced Error Characteristics of MM5 and WRF Operated in Climate Mode over the Alpine Region: An Ensemble-Based Analysis. *Journal of Climate*, **24 (12)**, 3107–3123, doi:10.1175/2011JCLI3674.1.

Bala Subrahamanyam, D., and T. J. Anurose, 2011: Solar eclipse induced impacts on sea/-land breeze circulation over Thumba: A case study. *Journal of Atmospheric and Solar-Terrestrial Physics*, **73 (5–6)**, 703–708, doi:10.1016/j.jastp.2011.01.002.

Bigelow, F. H., 1902: Eclipse meteorology and Allied problems. U.S. Department of Agriculture Weather Bureau Bulletin I 267, U.S. Department of Agriculture, Washington, 166 pp.

Birt, W., 1836: Meteorological observations made during the solar eclipse of May 15, 1836, at Greenwich. *Lond. Edinb. Phil. Mag.*, **9 (55)**, 393–394.

Browning, K., and R. Wexler, 1968: The determination of kinematic properties of a wind field using doppler radar. *Journal of Applied Meteorology*, **7 (1)**, 105–113.

Browning, K., and Coauthors, 1976: Structure of an Evolving Hailstorm Part V: Synthesis and implications for Hail Growth and Hail Suppression. *Monthly Weather Review*, **104 (5)**, 603–610, doi:10.1175/1520-0493(1976)104⟨0603:SOAEHP⟩2.0.CO;2.

Chin, S. H.-N., M. Leach, G. Sugiyama, and F. Aluzzi, 2001: A preliminary study of surface cold bias in COAMPS. *Preprints, Ninth Conference on Mesoscale Processes, Amer. Meteorol. Soc.*, 30 July – 2 August, Fort Lauderdale, FL.

Clayton, H. H., 1901: The eclipse cyclone and the diurnal cyclones. *Annals of the Astronomical Observatory of Harvard College*, **43 (1)**.

De Wekker, S. F. J., D. G. Steyn, and S. Nyeki, 2004: A Comparison Of Aerosol-Layer

And Convective Boundary-Layer Structure Over A Mountain Range During Staaarte '97. *Boundary-Layer Meteorology*, **113 (2)**, 249–271, doi:10.1023/B:BOUN.0000039371.41823.37.

Duine, G.-J., T. Hedde, P. Roubin, P. Durand, M. Lothon, F. Lohou, P. Augustin, and M. Fourmentin, 2017: Characterization of valley flows within two confluent valleys under stable conditions: Observations from the KASCADE field experiment. *Quarterly Journal of the Royal Meteorological Society*, **143 (705)**, 1886–1902, doi:10.1002/qj.3049.

Ek, M., and L. Mahrt, 1994: Daytime Evolution of Relative Humidity at the Boundary Layer Top. *Monthly Weather Review*, **122 (12)**, 2709–2721, doi:10.1175/1520-0493(1994)122⟨2709:DEORHA⟩2.0.CO;2.

Eugster, W., C. Emmel, S. Wolf, N. Buchmann, J. P. McFadden, and C. D. Whiteman, 2017: Effects of vernal equinox solar eclipse on temperature and wind direction in Switzerland. *Atmos. Chem. Phys.*, **17 (24)**, 14 887–14 904, doi:10.5194/acp-17-14887-2017.

Fernández, W., V. Castro, and H. Hildago, 1993: Air temperature and wind changes in Costa Rica during the total solar eclipse of July 11, 1991. *Earth, Moon, and Planets*, **63 (2)**, 133–147.

Founda, D., D. Melas, S. Lykoudis, I. Lisaridis, E. Gerasopoulos, G. Kouvarakis, M. Petrakis, and C. Zerefos, 2007: The effect of the total solar eclipse of 29 March 2006 on meteorological variables in Greece. *Atmos. Chem. Phys.*, **7 (21)**, 5543–5553, doi:10.5194/acp-7-5543-2007.

Gao, Y., J. Xu, and D. Chen, 2015: Evaluation of WRF Mesoscale Climate Simulations over the Tibetan Plateau during 1979–2011. *Journal of Climate*, **28 (7)**, 2823–2841, doi:10.1175/JCLI-D-14-00300.1.

Gray, S. L., and R. G. Harrison, 2012: Diagnosing eclipse-induced wind changes. *Proc. R. Soc. A*, **468 (2143)**, 1839–1850, doi:10.1098/rspa.2012.0007.

Gross, P., and A. Hense, 1999: Effects of a Total Solar Eclipse on the Mesoscale Atmospheric Circulation over Europe – A Model Experiment. *Meteorology and Atmospheric Physics*, **71 (3-4)**, 229–242, doi:10.1007/s007030050057.

Hanna, S. R., and R. Yang, 2001: Evaluations of Mesoscale Models' Simulations of Near-Surface Winds, Temperature Gradients, and Mixing Depths. *Journal of Applied Meteorology*, **40 (6)**, 1095–1104, doi:10.1175/1520-0450(2001)040⟨1095:EOMMSO⟩2.0.CO;2.

Hawkes, H., 1947: Mountain and valley winds with special reference to the diurnal mountain winds of the Great Salt Lake region. Ph.d. dissertation, Ohio State University, Columbus, OH, USA.

Henne, S., J. Dommen, B. Neininger, S. Reimann, J. Staehelin, and A. S. H. Prévôt, 2005a: Influence of mountain venting in the Alps on the ozone chemistry of the lower free troposphere and the European pollution export. *Journal of Geophysical Research: Atmospheres*, **110 (D22)**, D22 307, doi:10.1029/2005JD005936.

Henne, S., M. Furger, and A. H. Prévôt, 2005b: Climatology of mountain venting-induced elevated moisture layers in the lee of the Alps. *Journal of Applied Meteorology*, **44 (5)**, 620–633, doi:10.1175/JAM2217.1.

Henne, S., and Coauthors, 2004: Quantification of topographic venting of boundary layer air to the free troposphere. *Atmos. Chem. Phys.*, **4 (2)**, 497–509, doi:10.5194/acp-4-497-2004.

Jiménez, P. A., and J. Dudhia, 2011: Improving the representation of resolved and unresolved topographic effects on surface wind in the WRF model. *Journal of Applied Meteorology and Climatology*, **51 (2)**, 300–316, doi:10.1175/JAMC-D-11-084.1.

Jiménez, P. A., and J. Dudhia, 2013: On the Ability of the WRF Model to Reproduce the Surface Wind Direction over Complex Terrain. *Journal of Applied Meteorology and Climatology*, **52 (7)**, 1610–1617, doi:10.1175/JAMC-D-12-0266.1.

Jiménez, P. A., J. F. González-Rouco, E. García-Bustamante, J. Navarro, J. P. Montávez, J. V.-G. de Arellano, J. Dudhia, and A. Muñoz-Roldan, 2010: Surface Wind Regionalization over Complex Terrain: Evaluation and Analysis of a High-Resolution WRF Simulation. *Journal of Applied Meteorology and Climatology*, **49 (2)**, 268–287, doi:10.1175/2009JAMC2175.1.

Kaimal, J. C., and J. J. Finnigan, 1994: *Atmospheric boundary layer flows: their structure and measurement*. Oxford University Press.

Kalverla, P. C., G.-J. Duine, G.-J. Steeneveld, and T. Hedde, 2016: Evaluation of the Weather Research and Forecasting Model in the Durance Valley Complex Terrain during the KASCADE Field Campaign. *Journal of Applied Meteorology and Climatology*, **55 (4)**, 861–882, doi:10.1175/JAMC-D-15-0258.1.

Kossmann, M., U. Corsmeier, S. F. J. De Wekker, F. Fiedler, R. Vögtlin, N. Kalthoff, H. Güsten, and B. Neininger, 1999: Observations of handover processes between the atmospheric boundary layer and the free troposphere over mountainous terrain. *Contributions to Atmospheric Physics*, **72 (4)**, 329–350.

Kühnlein, C., A. Dörnbrack, and M. Weissmann, 2013: High-Resolution Doppler Lidar Observations of Transient Downslope Flows and Rotors. *Monthly Weather Review*, **141 (10)**, 3257–3272, doi:10.1175/MWR-D-12-00260.1.

Lenschow, D. H., L. L. Stankov, and L. Mahrt, 1979: The rapid morning boundary-layer transition. *Journal of the Atmospheric Sciences*, **36 (11)**, 2108–2124, doi:10.1175/1520-0469(1979)036⟨2108:TRMBLT⟩2.0.CO;2.

Li, J.-G., and B. W. Atkinson, 1999: Transition regimes in valley airflows. *Boundary-Layer Meteorology*, **91 (3)**, 385–411, doi:10.1023/A:1001846005338.

Lothon, M., and Coauthors, 2014: The BLLAST field experiment: Boundary-Layer Late Afternoon and Sunset Turbulence. *Atmos. Chem. Phys.*, **14 (20)**, 10 931–10 960, doi:10.5194/acp-14-10931-2014.

Mahrt, L., 1981: The early evening boundary layer transition. *Quarterly Journal of the Royal Meteorological Society*, **107 (452)**, 329–343, doi:10.1002/qj.49710745205.

McKendry, I. G., D. van der Kamp, K. B. Strawbridge, A. Christen, and B. Crawford, 2009: Simultaneous observations of boundary-layer aerosol layers with CL31 ceilometer and 1064/532 nm lidar. *Atmospheric Environment*, **43 (36)**, 5847–5852, doi:10.1016/j.atmosenv.2009.07.063.

Michioka, T., and F. K. Chow, 2008: High-resolution large-eddy simulations of scalar transport in atmospheric boundary layer flow over complex terrain. *Journal of Applied Meteorology and Climatology*, **47 (12)**, 3150–3169, doi:10.1175/2008JAMC1941.1.

Nadeau, D. F., E. R. Pardyjak, C. W. Higgins, H. Huwald, and M. B. Parlange, 2013: Flow during the evening transition over steep Alpine slopes. *Quarterly Journal of the Royal Meteorological Society*, **139 (672)**, 607–624, doi:10.1002/qj.1985.

Pal, S., T. R. Lee, S. Phelps, and S. F. J. De Wekker, 2014: Impact of atmospheric boundary layer depth variability and wind reversal on the diurnal variability of aerosol concentration at a valley site. *Science of The Total Environment*, **496**, 424–434, doi:10.1016/j.scitotenv.2014.07.067.

Pardyjak, E. R., H. J. S. Fernando, J. C. Hunt, A. A. Grachev, and J. Anderson, 2009: A case study of the development of nocturnal slope flows in a wide open valley and associated air quality implications. *Meteorologische Zeitschrift*, **18 (1)**, 85–100, doi:10.1127/0941-2948/2009/362.

Päschke, E., R. Leinweber, and V. Lehmann, 2015: An assessment of the performance of a 1.5 μm doppler lidar for operational vertical wind profiling based on a 1-year trial. *Atmospheric Measurement Techniques*, **8 (6)**, 2251.

Phelps, S., 2014: Representativeness of wind measurements in a complex terrain region in Southern Virginia. M.S. thesis, University of Virginia.

Piriou, J., and P. Lamboley, 1999: Prévision numérique des effets météorologiques d'une éclipse de soleil. *La Météorologie*, **8 (28)**, 52–56.

Prenosil, T., 2000: The influence of the 11 August 1999 total solar eclipse on the weather over central Europe. *Meteorologische Zeitschrift*, **9**, 351–359.

Sheskin, D. J., 1997: *Handbook of Parametric and Nonparametric Statistical Procedures*. CRC Press, Boca Raton, FL.

Stull, R. B., 1988: *An Introduction to Boundary Layer Meteorology*. Kluwer Academic Publishers, Dordrecht, 666 pp.

van den Bossche, M., and S. F. J. De Wekker, 2016: Spatiotemporal variability of surface meteorological variables during Fog and No-fog events in the Heber Valley, UT; Selected case studies from MATERHORN-Fog. *Pure and Applied Geophysics*, **9 (173)**, 3031–3048, doi:10.1007/s00024-016-1352-6.

Van Gorsel, E., 2003: Aspects of flow characteristics and turbulence in complex terrain. Ph.d. dissertation, University of Basel, Basel, Switzerland.

Vickers, D., and L. Mahrt, 1997: Quality control and flux sampling problems for tower and aircraft data. *J Atmos Ocean Tech*, **14 (3)**, 512–526.

Vogel, B., M. Baldauf, and F. Fiedler, 2001: The Influence of a solar eclipse on temperature and wind in the Upper-Rhine Valley – A numerical case study. *Meteorologische Zeitschrift*, **10 (3)**, 207–214, doi:10.1127/0941-2948/2001/0010-0207.

Weigel, A. P., and M. W. Rotach, 2004: Flow structure and turbulence characteristics of the daytime atmosphere in a steep and narrow Alpine valley. *Quarterly Journal of the Royal Meteorological Society*, **130 (602)**, 2605–2627, doi:10.1256/qj.03.214.

Whiteman, C. D., 1982: Breakup of temperature inversions in deep mountain valleys: Part I. Observations. *Journal of Applied Meteorology*, **21 (3)**, 270–289, doi:10.1175/1520-0450(1982)021⟨0270:BOTIID⟩2.0.CO;2.

Whiteman, C. D., 1989: Morning transition tracer experiments in a deep narrow valley. *Journal of Applied Meteorology*, **28 (7)**, 626–635, doi:10.1175/1520-0450(1989)028⟨0626:MTTEIA⟩2.0.CO;2.

Whiteman, C. D., 2000: *Mountain Meteorology: Fundamentals and Applications*. Oxford University Press, New York, 355 pp.

Whiteman, C. D., K. J. Allwine, L. J. Fritschen, M. M. Orgill, and J. R. Simpson, 1989: Deep valley radiation and surface energy budget microclimates. Part II: Energy budget. *Journal of Applied Meteorology*, **28 (6)**, 427–437, doi:10.1175/1520-0450(1989)028⟨0427:DVRASE⟩2.0.CO;2.

Whiteman, C. D., X. Bian, and S. Zhong, 1999: Wintertime evolution of the temperature inversion in the Colorado Plateau Basin. *Journal of Applied Meteorology*, **38 (8)**, 1103–1117, doi:10.1175/1520-0450(1999)038⟨1103:WEOTTI⟩2.0.CO;2.

Wilczak, J. M., S. P. Oncley, and S. A. Stage, 2001: Sonic anemometer tilt correction algorithms. *Boundary-Layer Meteorol*, **99 (1)**, 127–150.

Zardi, D., and C. D. Whiteman, 2013: Diurnal mountain wind systems. *Mountain Weather Research and Forecasting*, F. K. Chow, S. F. J. De Wekker, and B. J. Snyder, Eds., Springer Atmospheric Sciences, Springer Netherlands, 35–119, doi:10.1007/978-94-007-4098-3_2.

Zhong, S., and F. K. Chow, 2013: Meso- and fine-scale modeling over complex terrain: Parameterizations and applications. *Mountain Weather Research and Forecasting*, F. K. Chow, S. F. J. De Wekker, and B. J. Snyder, Eds., Springer Atmospheric Sciences, Springer Netherlands, 591–653, doi:10.1007/978-94-007-4098-3_10.

Zhong, S., and J. Fast, 2003: An Evaluation of the MM5, RAMS, and Meso-Eta Models at Subkilometer Resolution Using VTMX Field Campaign Data in the Salt Lake Valley. *Monthly Weather Review*, **131 (7)**, 1301–1322, doi:10.1175/1520-0493(2003)131⟨1301:AEOTMR⟩2.0.CO;2.